大阪公立大学
Osaka Metropolitan University
学術情報リポジトリ

Direct numerical simulation of turbulent heat transfer over fully resolved anisotropic porous structures

メタデータ	言語: eng 出版者: 公開日: 2020-09-24 キーワード (Ja): キーワード (En): 作成者: Nishiyama, Yudai, Kuwata, Yusuke, Suga, Kazuhiko メールアドレス: 所属:
URL	http://hdl.handle.net/10466/00017052

Direct numerical simulation of turbulent heat transfer over fully resolved anisotropic porous structures

Yudai Nishiyama, Yusuke Kuwata, Kazuhiko Suga*

Department of Mechanical Engineering, Osaka Prefecture University, Sakai, Osaka 599–8531, Japan

Abstract

Lattice Boltzmann direct numerical simulations of turbulent heat transfer over and inside anisotropic porous media settled on the bottom of a plane channel are performed at the bulk Reynolds number of 2900 for the isothermal and conjugate heat transfer wall conditions. Four different porous walls are considered. They are walls with only the wall-normal permeability, with the wall-normal and spanwise permeabilities, with the wall-normal and streamwise permeabilities, and with the isotropic wall-normal, spanwise and streamwise permeabilities. The porosity of the porous walls ranges from 0.6 to 0.8. Discussions on the effects of the anisotropic permeability on turbulent thermal fields are carried out by the instantaneous flow visualizations and the statistical quantities. In particular, temperature fluctuations, turbulent and dispersion heat fluxes are examined both inside and outside of the porous walls. Finally, the heat transfer performance is discussed considering the effects of the anisotropic permeability.

Keywords: Turbulent heat transfer, Channel flow, Anisotropic porous

---

*Corresponding author

Email address: `suga@me.osakafu-u.ac.jp` (Kazuhiko Suga)

wall, Lattice Boltzmann method, Direct numerical simulation

List of Symbols

D_1	square hole size
D_2	pitch of the square hole rows
$G_{\theta 2}$	fluid-phase $x-z$ plane-averaged temperature gradient: $\partial\left[\overline{\theta}\right]^{\mathrm{f}}/\partial y$
h	porous wall thickness: $0.7H$
H	clear channel height
H_j^{d}	fluid-phase $x-z$ plane-dispersion heat flux: $\left[\widetilde{\overline{u}}_j\widetilde{\overline{\theta}}\right]^{\mathrm{f}}$
H_j^{t}	fluid-phase $x-z$ plane-averaged turbulent heat flux: $\left[\overline{u'_j\theta'}\right]^{\mathrm{f}}$
K_{ij}	permeability tensor
Nu	Nusselt number
$p(\theta', {\omega'}_z)$	joint probability density function of θ' and ${\omega'}_z$
Pr	Prandtl number
P_θ	production of the fluid-phase $x-z$ plane-averaged temperature variance: $-\left[\overline{v'\theta'}\right]^{\mathrm{f}}\partial\left[\overline{\theta}\right]^{\mathrm{f}}/\partial y$
$\overline{q_{\mathrm{w}}^{\mathrm{p}}}$	averaged heat flux on the porous interface
Q_i	quadrant of the turbulent heat flux
$\mathrm{Re_b}$	bulk Reynolds number: $U_{\mathrm{b}}H/\nu$
R_{ij}	plane averaged Reynolds stress: $\left[\overline{u'_j u'_j}\right]^{\mathrm{f}}$
Re_K	permeability Reynolds number
Re_K^{**}	surrogate permeability Reynolds number

$\mathrm{Re}_\tau^\mathrm{p}$	friction Reynolds number of the porous interface: $u_\tau^\mathrm{p}\delta^\mathrm{p}/\nu$
$\mathrm{Re}_\tau^\mathrm{t}$	friction Reynolds number of the top smooth wall: $u_\tau^\mathrm{t}\delta^\mathrm{t}/\nu$
t	time
$\mathcal{T}_{12}$	plane-dispersion stress: $[\tilde{\tilde{u}}\tilde{\tilde{v}}]^\mathrm{f}$
u_i	velocity
u_τ^p	friction velocity on the porous interface
u_τ^t	friction velocity on the top smooth wall
U_b	bulk mean velocity
W_p	pumping power coefficient
x, y, z	streamwise, vertical and spanwise coordinates
II	second invariant of the velocity gradient tensor: $-2(\partial u_i/\partial x_j)(\partial u_j/\partial x_i)$
γ_f	fluid thermal diffusivity
γ_s	solid thermal diffusivity
δ^p	boundary layer thickness over porous wall
δ^t	boundary layer thickness over top smooth wall
$\mathit{\Delta}^\mathrm{c}$	coarser grid spacing
$\mathit{\Delta}^\mathrm{f}$	finer grid spacing
$\mathit{\Delta}\Theta$	temperature difference: $\Theta_\mathrm{w} - \Theta_0$
θ	temperature
θ^*	$(\theta - \Theta_0)/\Delta\Theta$
Θ_f	fluid-phase $x - z$ plane-averaged mean temperature: $\left[\overline{\theta}\right]^\mathrm{f}$

$\theta'_{\mathrm{f_{rms}}}$	fluid-phase $x-z$ plane-averaged root mean square of the temperature variance: $\sqrt{\left[\overline{\theta'\theta'}\right]^{\mathrm{f}}}$
Θ_{p}	mean temperature of the porous interface
Θ_{s}	solid-phase $x-z$ plane-averaged mean temperature: $\left[\overline{\theta}\right]^{\mathrm{s}}$
$\theta'_{\mathrm{s_{rms}}}$	solid-phase $x-z$ plane-averaged root mean square of the temperature variance: $\sqrt{\left[\overline{\theta'\theta'}\right]^{\mathrm{s}}}$
Θ_0	top wall temperature
Θ_{w}	porous or bottom wall temperature
θ_τ^{p}	friction temperature on the porous interface
θ_τ^{t}	friction temperature on the top smooth wall
ν	kinematic viscosity
ρ	fluid density
φ	porosity
ϕ	variable
$\overline{\phi}$	Reynolds averaged value of ϕ
ϕ'	fluctuation of ϕ: $\phi - \overline{\phi}$
$[\phi]^{\mathrm{f}}$	fluid phase plane-averaged value of ϕ
$[\phi]^{\mathrm{s}}$	solid phase plane-averaged value of ϕ
$\tilde{\phi}$	dispersion of ϕ: $\phi - [\phi]^{\mathrm{f}}$
ψ	plane porosity
ω_z	spanwise vorticity

$(\cdot)^{\mathrm{p+}}$ normalized value by the friction velocity or the friction temperature on the porous interface

$(\cdot)^{*}$ normalized value by the bulk mean velocity or the temperature difference

1. Introduction

Porous media consisting of many interconnected voids have large specific surface areas, and this characteristic can be utilized in many engineering devices. Correspondingly, it is widely understood that turbulent heat and fluid flow phenomena in interface regions of porous media (over and underneath of the interfaces between porous and clear channel flow regions) play key roles in designing and optimizing those devices.

For turbulent flows over porous interfaces, experimental studies (e.g. Lovera and Kennedy, 1969; Ruff and Gelhar, 1972; Ho and Gelhar, 1973; Zagni and Smith, 1976; Zippe and Graf, 1983; Kong and Schetz, 1982; Shimizu et al., 1990; Pokrajac and Manes, 2009; Manes et al., 2009; Detert et al., 2010; Suga et al., 2010, 2011, 2013; Manes et al., 2011) revealed the fact that the wall permeability affects the near-wall turbulent flow structure and enhances momentum exchange across the porous surfaces. This results from mainly that turbulence is not significantly damped near the porous wall and the penetration of eddy vortex motions into the porous wall is allowed by the permeability. The direct numerical simulation (DNS) studies (Breugem and Boersma, 2005; Breugem et al., 2006; Kuwata and Suga, 2016b) and the particle image velocimetry (PIV) experiments (Suga et al., 2010, 2011, 2017b; Suga, 2016) for turbulent channel flows over isotropic porous media suggested that there were correlations between the inner turbulence characteristics and the permeability Reynolds number ($\mathrm{Re}_K = u_\tau^{\mathrm{p}}\sqrt{K}/\nu$) which is based on the friction velocity u_τ^{p} on the porous wall, the wall permeability K and the fluid kinematic viscosity ν. Those DNS and PIV studies confirmed that the streaky turbulence structure was destroyed above highly permeable walls due to the downward motions into the wall by the Kelvin–Helmholtz (K–H) instability generated at the porous surface.

Through the budget term analysis of the volume-averaged turbulence equation, Kuwata and Suga (2016c) provided the detailed distribution profiles of turbulence and dispersion terms appearing in the double (volume and Reynolds) averaged Navier-Stokes (DANS) equations. They analysed the data of Kuwata and Suga (2016b) for turbulent isotropic porous walled channel flows with the wall porosity of $\varphi = 0.71$ at the bulk Reynolds number of $\mathrm{Re}_\mathrm{b} \simeq 3000$. They showed that compared with the Reynolds stresses, the levels of the wall-normal and spanwise components of the dispersion stress were far smaller though the streamwise component keeps the same level. The drag force was the main source for the dispersion instead of the mean shear inside the porous layer and the gained energy was partly transferred to the turbulent kinetic energy.

In the thermal field, the DNS study by Chandesris et al. (2013) confirmed that compared to a smooth solid wall case, larger vortical structures created above the porous layer significantly increased turbulent heat flux. The simulated thermal fields were at the fluid Prandtl number (Pr) of 0.1 with the same flow conditions as those of Breugem and Boersma (2005). They were for isotropic porous walled turbulent channel flows at $\mathrm{Re}_\mathrm{b} = 5500$ over fully resolved levitating cube arrays with $\varphi = 0.875$. It was found that deeply inside the porous layer until approximately four rows of the cubes, an influence of such large scale structures was detected even at such a low Prandtl number. The root mean square (rms) temperature fluctuation profiles showed a strong peak inside the porous layer. It was then concluded that this peak was not related to turbulent mixing, but to large scale pressure waves penetrating deeply inside the porous layer while a similar behavior was not observed for velocity fluctuations due to the drag effects.

When the porous structure becomes anisotropic, we should consider the wall permeability as a second rank tensor quantity. Since the anisotropic permeability is expected to be a key factor to control the flows around porous media, several studies have focused on flows over anisotropic porous media. The DNS study by Kuwata and Suga (2017) considered structures designed ideally to have anisotropic components of the permeability tensor. The considered four cases were walls with square pore arrays aligned with the Cartesian axes, namely walls with only the wall-normal diagonal component, with the wall-normal and spanwise diagonal components, with the wall-normal and streamwise diagonal components, and with the isotropic wall-normal, spanwise and streamwise diagonal components of the permeability tensor. The porosities of the considered porous media were $\varphi = 0.6 - 0.8$ and the bulk flow Reynolds numbers were $\mathrm{Re_b} = 2200 - 5900$. They found that turbulence was not significantly changed by the wall-normal diagonal component of the permeability tensor (called the wall-normal permeability, hereafter for simplicity) itself while the streamwise and spanwise components (streamwise and spanwise permeabilities, hereafter) considerably contributed to enhance turbulence over the porous media. The turbulence enhancement was more obvious by the streamwise permeability. Suga et al. (2018) experimentally confirmed this trend by measuring turbulence over anisotropic porous media whose porosities were 0.7 and wall-normal permeability was designed to be larger than the other components by factors of 1.2, 1.5 and 173 at $\mathrm{Re_b} = 900 - 13600$. The DNS by Rosti et al. (2018) also considered anisotropic permeability effects. In their results, very interestingly, some anisotropic cases showed even lower drag coefficients than those over solid smooth walls. Since they imposed a very smaller permeability in the wall-normal direction than those in the other directions, the K–H instability was mitigated in their simulations. Due to the combined effect of the slip velocity and the mitigation of the K–H instability, the drag reduction phenomenon was predicted. However, when realistic porous structures are considered, the effect of the surface topology, which relates to the surface roughness, may not be ignored. Such an effect on flows was not considered in their momentum transfer condition applied to the porous interface to connect the volume averaged Navier-Stokes (VANS) equations (Whitaker, 1986, 1996) for the porous layers. They modified the momentum transfer condition form of Ochoa-Tapia and Whitaker (1995) neglecting a term representing the drag by the surface texture.

Although heat transfer at the porous interface is an important issue in engineering, to the best of the authors' knowledge, there is no report in the literature for turbulent heat transfer focusing on anisotropic effects of porous media. Therefore, this study performs DNSs of turbulent forced convection in porous-walled channel flows at $\mathrm{Re_b} = 2900$ by the lattice Boltzmann method (LBM) as a follow-up study of Kuwata and Suga (2017). To understand the effects of anisotropic permeabilities on the turbulent thermal fields both inside and outside the porous walls, the four distinctive anisotropic porous media of Kuwata and Suga (2017) are considered. They are namely walls with only the wall-normal permeability, with the wall-normal and spanwise permeabilities, with the wall-normal and streamwise permeabilities, and with the isotropic wall-normal, spanwise and streamwise permeabilities. The porosities of the considered porous media are thus $\varphi = 0.6 - 0.8$. Two different thermal wall boundary conditions: isothermal and conjugate heat transfer conditions for the porous layer, are considered to discuss turbulent heat transfer over and inside the porous walls.

2. Numerical scheme

2.1. Flow fields

In the present study, DNSs are performed by the D3Q27 multiple-relaxation-time LBM (MRT-LBM) (Suga et al., 2015) for the flow fields. The time evolution equation of the distribution function $\boldsymbol{f}$ can be written as

$$|\boldsymbol{f}(\boldsymbol{x}+\boldsymbol{\xi}_\alpha \delta t, t+\delta t)\rangle - |\boldsymbol{f}(\boldsymbol{x},t)\rangle = -\boldsymbol{M}^{-1}\hat{\boldsymbol{S}}(|\boldsymbol{m}(\boldsymbol{x},t)\rangle - |\boldsymbol{m}^{\mathrm{eq}}(\boldsymbol{x},t)\rangle) - |\boldsymbol{F}(\boldsymbol{x},t)\rangle\,, \tag{1}$$

where $\boldsymbol{\xi}_\alpha$ is the discrete velocity, notations such as $|\boldsymbol{f}\rangle$ is $|\boldsymbol{f}\rangle = (f_0, f_1, \ldots, f_{26})^{\mathrm{T}}$ and δt is the time step. The parameters of the D3Q27 discrete velocity model are listed in Table 1 in which the sound speed is $c_{\mathrm{s}}/c = 1/\sqrt{3}$ with the particle velocity $c = \mathit{\Delta}/\delta t$, the lattice spacing $\mathit{\Delta}$, and the weighting factor w_α. The term $\boldsymbol{F}$ is the external force. The matrix $\boldsymbol{M}$ is a 27×27 matrix which linearly transforms the distribution functions to the moments as $|\boldsymbol{m}\rangle = \boldsymbol{M}\,|\boldsymbol{f}\rangle$.

The equilibrium moment $|\boldsymbol{m}^{\mathrm{eq}}\rangle = \boldsymbol{M}\,|\boldsymbol{f}^{\,\mathrm{eq}}\rangle$ and the transformation matrix $\boldsymbol{M}$ are listed in Tables 2 and 3. The local equilibrium distribution function $\boldsymbol{f}^{\,\mathrm{eq}}$ is obtained as

$$f_\alpha^{\mathrm{eq}} = w_\alpha \left\{ \rho + \rho_0 \left(\frac{\boldsymbol{\xi}_\alpha \cdot \boldsymbol{u}}{c_\mathrm{s}^2} + \frac{(\boldsymbol{\xi}_\alpha \cdot \boldsymbol{u})^{\,2} - c_\mathrm{s}^2 |\boldsymbol{u}|^2}{2c_\mathrm{s}^4} \right) \right\}, \tag{2}$$

where $\boldsymbol{u}$ is the fluid velocity vector and the density ρ is expressed as the summation of constant and fluctuation parts, $\rho = \rho_0 + \delta\rho$ (He and Luo, 1997). The collision matrix $\hat{\boldsymbol{S}}$ is diagonal:

$$\begin{aligned} \hat{\boldsymbol{S}} \equiv &\mathrm{diag}(0, 0, 0, 0, s_4, s_5, s_7, s_7, s_7, s_{10}, s_{10}, s_{10}, \\ &s_{13}, s_{13}, s_{13}, s_{16}, s_{17}, s_{18}, s_{18}, s_{20}, s_{20}, s_{20}, s_{23}, s_{23}, s_{23}, s_{26}). \end{aligned} \tag{3}$$

The relaxation parameters presently applied are from Suga et al. (2015):

$$\begin{aligned} s_4 = 1.54,\ \ s_7 = s_5,\ \ s_{10} = 1.5,\ \ s_{13} = 1.83,\ \ s_{16} = 1.4, \\ s_{17} = 1.61,\ \ s_{18} = s_{20} = 1.98,\ \ s_{23} = s_{26} = 1.74. \end{aligned} \tag{4}$$

The relaxation parameter s_5 is related to the kinematic viscosity ν,

$$\nu = c_\mathrm{s}^2 \left(\frac{1}{s_5} - \frac{1}{2} \right) \delta t. \tag{5}$$

The macroscopic variables such as the density $\rho = m_0$, the momentum $\rho_0 u_i = m_i$ and the pressure p are $\rho = \Sigma_\alpha f_\alpha$, $\rho_0 u_i = \Sigma_\alpha \boldsymbol{\xi}_{\alpha i} f_\alpha$ and $p = c_\mathrm{s}^2 \rho$, respectively. The applied numerical scheme was validated by Suga et al. (2015) through the application of the turbulent channel flow at $\mathrm{Re}_\tau = 180$. It was confirmed that the predicted turbulence statistics such as the mean velocity, Reynolds stresses, budget terms of the turbulent kinetic energy, and energy spectra agreed almost perfectly with those of the spectral method by Kim et al. (1987).

2.2. Thermal fields

For the thermal fields, the D3Q19 regularized single-relaxation-time LBM (SRT-LBM) for a passive scalar (He et al., 1998) is applied. The time evolution equation of the internal energy density distribution function $\boldsymbol{g}$ can be written as

$$|\boldsymbol{g}(\boldsymbol{x}+\boldsymbol{\xi}_\alpha \delta t, t+\delta t)\rangle - |\boldsymbol{g}(\boldsymbol{x},t)\rangle = -\frac{1}{\tau_g}\left(|\boldsymbol{g}(\boldsymbol{x},t)\rangle - |\boldsymbol{g}^{\mathrm{eq}}(\boldsymbol{x},t)\rangle\right), \tag{6}$$

where τ_g is the relaxation time and $\boldsymbol{g}^{\mathrm{eq}}$ is the equilibrium part of the distribution function $\boldsymbol{g}$. The parameters for the D3Q19 discrete velocity model are listed in Table 4. Temperature θ and the equilibrium part $\boldsymbol{g}^{\mathrm{eq}}$ are respectively written as

$$\theta = \sum_\alpha g_\alpha, \tag{7}$$

and

$$g_\alpha^{\mathrm{eq}} = w_\alpha \theta \left(1 + \frac{\boldsymbol{\xi}_\alpha \cdot \boldsymbol{u}}{c_{\mathrm{s}}^2}\right). \tag{8}$$

To stabilize the calculation at a high Reynolds number, the regularization process (Latt and Chopard, 2006) is introduced as

$$|\boldsymbol{g}(\boldsymbol{x}+\boldsymbol{\xi}_\alpha \delta t, t+\delta t)\rangle = |\boldsymbol{g}^{\mathrm{eq}}(\boldsymbol{x},t)\rangle + \left(1-\frac{1}{\tau_g}\right)\left|\widehat{\boldsymbol{g}^{\mathrm{neq}}}(\boldsymbol{x},t)\right\rangle, \tag{9}$$

where $\widehat{\boldsymbol{g}^{\mathrm{neq}}}$ is the regularized non-equilibrium part of the distribution function $\boldsymbol{g}$. It is written as

$$\widehat{g_\alpha^{\mathrm{neq}}} = \frac{w_\alpha}{c_{\mathrm{s}}^2}\xi_{\alpha i}\sum_\beta g_\beta^{\mathrm{neq}}\xi_{\beta i} + \frac{w_\alpha}{2c_{\mathrm{s}}^4}\left(\xi_{\alpha i}\xi_{\alpha j} - c_{\mathrm{s}}^2\delta_{ij}\right)\sum_\beta g_\beta^{\mathrm{neq}}\xi_{\beta i}\xi_{\beta j}. \tag{10}$$

The thermal diffusivity of the fluid γ_{f} is related to the relaxation time τ_g as

$$\gamma_{\mathrm{f}} = c_{\mathrm{s}}^2\left(\tau_g - \frac{1}{2}\right)\delta t. \tag{11}$$

See Suga et al. (2017a) for the numerical details of the thermal field model.

2.3. Boundary conditions

The standard half-way bounce-back scheme is applied to the fluid-solid interface for the non-slip flow condition. For the isothermal solid phase condition, the scheme by Yoshida and Nagaoka (2010) is applied to the wall surfaces:

$$g_\alpha(\boldsymbol{x}, t+\delta t) = -g_\beta(\boldsymbol{x}, t) + \mathcal{E}\,\mathit{\Phi}_{\mathrm{w}}, \tag{12}$$

where $\mathit{\Phi}_{\mathrm{w}}$ is the wall temperature, $\boldsymbol{\xi}_\alpha = -\boldsymbol{\xi}_\beta$, and $\mathcal{E} = 2w_\alpha$ for the D3Q19 model.

To impose the conjugate heat transfer conditions, this study applies the half lattice division scheme of (Wang et al., 2007) which prescribes the conjugate heat transfer condition at the middle between the fluid and solid node points by the simple streaming process as follows:

$$g^{\mathrm{fluid}}(\boldsymbol{x} + \boldsymbol{\xi}_\alpha \delta t, t+\delta t) = g^{\mathrm{solid}}(\boldsymbol{x}, t), \tag{13}$$

$$g^{\mathrm{solid}}(\boldsymbol{x} + \boldsymbol{\xi}_\alpha \delta t, t+\delta t) = g^{\mathrm{fluid}}(\boldsymbol{x}, t). \tag{14}$$

3. Flow geometry and computational conditions

Figure 1 illustrates a schematic view of a porous-walled channel flow configuration. As shown in Fig. 1(a), the computational domain in the streamwise (x) × wall-normal (y) × spanwise (z) directions is $7.0H \times (H+h) \times 3.5H$. Here, H and $h = 0.7H$ are the clear channel height and porous layer thickness, respectively, and an impermeable smooth wall is considered at $y = H$. The origin of the wall-normal coordinate is set to the porous layer interface. Although the large-scale streamwise perturbation due to the K–H instability develops over the present porous layer, the streamwise computational domain length is confirmed to be sufficiently large to capture the turbulence statistics presently focused on. (See Appendix B for the discussion on the domain size.) For the porous media, three different anisotropic porous media (case Y, YZ, and XY) and the isotropic porous medium (case XYZ) are considered as shown in Fig. 1 (c). Those porous media have square holes, and the hole size and distance between holes are $D_1 = 0.12H$ and $D_2 = 1.3D_1$, respectively. All cases have the vertical square holes. In addition to the vertical holes, the streamwise and spanwise holes are made in cases XY and YZ, respectively. For case XYZ, the streamwise, vertical, and spanwise holes are made. The porous media under consideration are identical to those of Kuwata and Suga (2017). The parameters of the porous media: porosity φ and diagonal components of the permeability tensor K_{ij} are listed in Table 5. Note that those anisotropic porous media are categorized in the orthotropic porous media which only have diagonal components of the permeability tensor.

Using the imbalance-correction (IBC) zonal grid refinement method of Kuwata and Suga (2016a), the computational domain is decomposed into finer and coarser resolution domains. (Details for the thermal field IBC are described in Appendix A.) The grid node numbers of the finer mesh for the porous layer and the coarser mesh for the channel core are $1601(x) \times 217(y) \times 801(z)$ and $801(x) \times 88(y) \times 401(z)$, respectively. The normalized values of D_1 and the grid spacings of the coarser and finer grid regions, $\varDelta^{\mathrm{c}}$ and $\varDelta^{\mathrm{f}}$, are also listed in Table 5. Note that the superscripts "t+" and "p+" denote the normalized values by the viscous scales of the top and porous walls, respectively. The grid resolution of the finer mesh is set to $\varDelta^{\mathrm{f,p+}} < 2.0$ which is comparable to those employed in the previous DNS studies by the LBM (e.g. Bespalko et al., 2012; Kuwata and Suga, 2017). The grid independence test of the simulation was confirmed by comparing the obtained turbulent intensities with those by the 1.5 times finer mesh in each direction. The difference between the results was less than a few per cent and confirmed to be negligible.

In all cases, periodic boundary conditions are imposed in the streamwise and spanwise directions with a constant streamwise pressure difference. The no-slip boundaries are applied to the fluid-solid interfaces and two thermal wall boundary conditions are considered in the present study. For the isothermal wall boundary condition, as shown in Fig. 1 (a) constant low and high temperatures, denoted respectively as $\mathit{\Theta}_0$ and $\mathit{\Theta}_{\rm w}$, are respectively applied to the top smooth wall and the whole porous layer while for the conjugate heat transfer, as shown in Fig. 1 (b) a constant high temperature $\mathit{\Theta}_{\rm w}$ is applied only to the very bottom surface under the porous layer. The thermal diffusivity ratio of the solid to the fluid is $\gamma_{\rm s}/\gamma_{\rm f} = 4.4$. The Prandtl number of the working fluid is set to be $\mathrm{Pr} = 0.71$. In the following discussions, the superscript "*" indicates a value normalized by the bulk mean velocity $U_{\rm b}$ or the temperature difference $\mathit{\Delta}\Theta = \mathit{\Theta}_{\rm w} - \mathit{\Theta}_0$. The notations "-I" and "-C" mean the isothermal and conjugate wall boundary conditions, respectively.

The bulk Reynolds number $\mathrm{Re}_{\rm b} = U_{\rm b}H/\nu$, the permeability Reynolds number $\mathrm{Re}_K = u_\tau^{\rm p}\sqrt{K_{kk}/3}/\nu$, the friction Reynolds number for the smooth top wall $\mathrm{Re}_\tau^{\rm t} = u_\tau^{\rm t}\delta^{\rm t}/\nu$, and for the porous wall $\mathrm{Re}_\tau^{\rm p} = u_\tau^{\rm p}\delta^{\rm p}/\nu$ are listed in Table 6. Since the averaged shear stress at the top wall $\tau_{\rm w}^{\rm t}$ is calculated directly, the friction velocity at the top wall, $u_\tau^{\rm t} = \sqrt{\tau_{\rm w}^{\rm t}/\rho}$, can straightforwardly be derived. To characterize inner turbulence over porous media, many studies in the literature successfully applied the friction velocity at the porous wall interface. Following those DNS studies (Breugem et al., 2006; Chandesris et al., 2013; Rosti et al., 2015; Kuwata and Suga, 2016b,c) and experimental studies (White and Nepf, 2007; Manes et al., 2009; Pokrajac and Manes, 2009; Manes et al., 2011; Suga et al., 2018), the friction velocity at the porous wall is given by the momentum balance in the clear flow region, which means that the pressure drop $\mathit{\Delta} P$ is balanced with the wall-shear stress at the top wall $\tau_{\mathrm{w}}^{\mathrm{t}}$ and total shear stress at the porous wall $\tau_{\mathrm{w}}^{\mathrm{p}}$ including the viscous stress, Reynolds shear stress and plane-dispersion stress as follows:

$$L_x(\tau_{\mathrm{w}}^{\mathrm{t}} + \tau_{\mathrm{w}}^{\mathrm{p}}) = H\mathit{\Delta} P, \quad 0 \leq y \leq H. \tag{15}$$

This yields the friction velocity at the porous interface as follows:

$$u_\tau^{\mathrm{p}} = \sqrt{-(u_\tau^{\mathrm{t}})^2 + \frac{H\mathit{\Delta} P}{L_x \rho}}. \tag{16}$$

Following Breugem et al. (2006), the boundary layer thickness for the smooth top or porous walls, δ^{t} or δ^{p}, is defined as the distance from the solid or porous walls to the location where the total shear stress goes to zero. The total shear stress τ_a in the clear flow region can be obtained from integral of the momentum equation as follows:

$$\tau_a = \tau_{\mathrm{w}}^{\mathrm{p}} - \frac{y}{H}(\tau_{\mathrm{w}}^{\mathrm{p}} - \tau_{\mathrm{w}}^{\mathrm{t}}). \tag{17}$$

Thus, δ^{p}/H can be obtained by substituting $\tau_a = 0$ into the above equation:

$$\frac{\delta^{\mathrm{p}}}{H} = \frac{\tau_{\mathrm{w}}^{\mathrm{p}}}{\tau_{\mathrm{w}}^{\mathrm{t}} + \tau_{\mathrm{w}}^{\mathrm{p}}}. \tag{18}$$

The boundary layer thicknesses for the smooth top can be obtained as follows:

$$\frac{\delta^{\mathrm{t}}}{H} = 1 - \frac{\delta^{\mathrm{p}}}{H} = \frac{\tau_{\mathrm{w}}^{\mathrm{t}}}{\tau_{\mathrm{w}}^{\mathrm{t}} + \tau_{\mathrm{w}}^{\mathrm{p}}}. \tag{19}$$

The friction temperature at the top wall θ_τ^{t} is calculated directly as

$$\theta_\tau^{\mathrm{t}} = \frac{\overline{q_{\mathrm{w}}^{\mathrm{t}}}}{\rho c_{\mathrm{p}} u_\tau^{\mathrm{t}}}, \tag{20}$$

where $\overline{q_{\mathrm{w}}^{\mathrm{t}}}$ is the averaged heat flux at the top wall and c_{p} is the specific heat capacity. The friction temperature at the porous interface θ_τ^{p} can be estimated from the energy conservation in the vertical direction of the present system where the averaged heat fluxes at the top and porous walls, $\overline{q_{\mathrm{w}}^{\mathrm{t}}}$ and $\overline{q_{\mathrm{w}}^{\mathrm{p}}}$, have the same value. Therefore, θ_τ^{p} can be calculated as

$$\theta_\tau^{\mathrm{p}} = \frac{\overline{q_{\mathrm{w}}^{\mathrm{p}}}}{\rho c_{\mathrm{p}} u_\tau^{\mathrm{p}}} = \frac{\overline{q_{\mathrm{w}}^{\mathrm{t}}}}{\rho c_{\mathrm{p}} u_\tau^{\mathrm{p}}}. \tag{21}$$

4. Results and discussions

4.1. Instantaneous flow and thermal fields

To see the influence of the anisotropic permeability on turbulent vortices over the porous layer, Figs. 2 and 3 visualize iso-surfaces of $II^* = II/(U_{\mathrm{b}}/H)^2 = 15$ for the cases with the isothermal wall and conjugate heat transfer conditions, respectively. Here, II is the second invariant of the velocity gradient tensor. They are colored by the local instantaneous temperatures of $0 < \theta^* < 1.0$. At this threshold value, a very limited number of vortex tubes are detected in case Y-I (Fig. 2 (a)), although much more vortex tubes are observed in the other cases. Most vortex tubes are seen in the region over the porous interfaces than in the vicinity of the top smooth walls as reported by Kuwata and Suga (2017). In case YZ-I (Fig. 2 (b)), streak-like vortex structures seem to be developing over the porous interface and in cases XY-I and XYZ-I (Fig. 2 (c, d)) with the streamwise permeability, larger amount of vortex tubes with high temperatures exist over the porous interface, and they occasionally reach near the top smooth wall. It is then obvious that the streamwise permeability induces more vortex tubes than the spanwise permeability. Figure 3, which selects cases Y-C and XYZ-C to show typical temperature distributions, also shows surface temperatures of the porous structures with the conjugate heat transfer condition. Obviously, temperature gradients are seen in the vertical direction of the porous layer. Since the interfacial temperatures in the conjugate heat transfer condition become lower than those of the isothermal wall boundary condition, the range of the vortex temperatures becomes narrower and thus the visualized vortex temperatures look almost constant although they are not constant.

The contours of instantaneous fluctuations of the vertical velocity and temperature across the x–y planes, which are located at the centers of the square holes as illustrated in Fig. 4, are shown in Figs. 5 and 6. Note that each thermal field visualization is made at the same instant as that for the flow field. The sampled instant is chosen randomly after the flow is fully developed. Velocity penetrations are clearly seen in the porous layers in cases XY and XYZ (Fig. 5 (c, d)). They are induced by the Kelvin–Helmholtz instability originating from the inflection point of the mean streamwise velocity (Raupach et al., 1991; Finnigan, 2000). Although the vertical velocity fluctuations over the porous wall penetrate deeply inside the porous layer and reach near the bottom of the porous layer in cases XY and XYZ, the temperature fluctuations with the isothermal wall boundary condition are limited to the region up to $y \simeq -D_2$. In contrast to the temperature fluctuations for the isothermal cases, Fig. 6 shows deeper penetrations for the conjugate heat transfer cases even in case YZ-C (Fig. 6 (b)) in which the velocity fluctuations do not penetrate deeply compared with those in cases XY-C and XYZ-C (Fig. 6 (c, d)). However, clear difference in the penetrations of the temperature fluctuations between the isothermal (Fig. 5 (a)) and conjugate heat transfer (Fig. 6 (a)) cases cannot be observed.

4.2. Turbulence statistics

To examine the contribution of the thermal boundary conditions to heat transfer around the porous walls, the double (Reynolds and the x–z plane) averaging is applied to the energy equation. The fluid-phase plane averaging of a variable $\phi(x, y, z)$ is defined as

$$[\phi(y)]^{\mathrm{f}} = \frac{1}{\Delta S_{\mathrm{f}}} \int_{\Delta S_{\mathrm{f}}} \phi(x, y, z) \mathrm{d}s, \tag{22}$$

where ΔS_{f} is the fluid area contained within the averaging area ΔS of the x–z plane. Following Whitaker (1996), the double-averaged energy equation for the fluid phase can be written as

$$\begin{aligned} \frac{\partial \left[\overline{\theta}\right]^{\mathrm{f}}}{\partial t} + \left[\overline{u_j}\right]^{\mathrm{f}} \frac{\partial \left[\overline{\theta}\right]^{\mathrm{f}}}{\partial x_j} \quad = \quad & \underbrace{\frac{1}{\psi} \frac{\partial}{\partial x_j} \left(\gamma_{\mathrm{f}} \frac{\partial \psi \left[\overline{\theta}\right]^{\mathrm{f}}}{\partial x_j} \right)}_{\text{viscous diffusion}} \\ & - \frac{1}{\psi} \frac{\partial}{\partial x_j} \left(\psi \underbrace{\left[\overline{u_j'\theta'}\right]^{\mathrm{f}}}_{H_j^{\mathrm{t}}} + \psi \underbrace{\left[\overline{\tilde{\overline{u}}_j \tilde{\overline{\theta}}}\right]^{\mathrm{f}}}_{H_j^{\mathrm{d}}} \right) \\ & + \underbrace{\frac{1}{\psi} \frac{\partial}{\partial x_j} \left(\frac{1}{\Delta S} \oint_{\Delta S_{\mathrm{f}}} n_j \gamma_{\mathrm{f}} \bar{\theta} \mathrm{d}\ell \right)}_{\text{tortuosity}} \\ & + \underbrace{\frac{1}{\Delta S_{\mathrm{f}}} \oint_{\Delta S_{\mathrm{f}}} n_j \gamma_{\mathrm{f}} \frac{\partial \bar{\theta}}{\partial x_j} \mathrm{d}\ell,}_{\text{wall heat transfer}} \end{aligned} \tag{23}$$

where ℓ represents the circumference length of the solid obstacle within an averaging surface and n_j is its unit normal vector pointing outward from the fluid to solid phases. The plane porosity is defined as $\psi = \Delta S_{\mathrm{f}}/\Delta S$. For the Reynolds averaging, simulations are carried out over 30 turn over times after the flows reach fully developed state. This time duration is confirmed to be long enough by comparing the results with those by 45 turn over times. Note that since this study considers passive scaler transport, turbulent flow field statistics are not influenced by the difference of the thermal boundary conditions.

4.2.1. Flow field statistics

Although detailed discussions on the flow field for the same porous media were carried out by Kuwata and Suga (2017), we briefly review the flow field statistics for the sake of completeness of the following discussions.

Figure 7 presents profiles of the fluid-phase x–z plane-averaged streamwise mean velocity $U^{\mathrm{p}+} = [\bar{u}]^{\mathrm{f}} / u_{\tau}^{\mathrm{p}}$. In Fig. 7 (a), the profiles in cases YZ, XY, and XYZ are significantly skewed due to the increased turbulent friction at the porous wall (Breugem et al., 2006; Suga et al., 2010), while that in case Y is almost symmetry, suggesting that the effects of the porous wall in case Y are marginal. As a decrease in the inner-scaled mean velocity represents an increase in the turbulent friction, the turbulent drag is the maximum in case XYZ, followed by cases XY and YZ. This can be confirmed in the friction Reynolds numbers in Table 6 because the bulk mean Reynolds number is almost the same in all the cases. Figure 7(b) shows positive slip velocities at the porous wall interfaces in all the cases, and the inflection points of the profiles beneath the porous interfaces. Such an inflection point is the necessary condition for the inviscid instability: the K–H instability (Drazin and Howard, 1966). However, the mean velocity profiles beneath the porous interface are very different; the streamwise mean flow is confined to the region of $-1 < y/D_2 < 0$ in cases Y and YZ while the porous wall in cases XY and XYZ allows the streamwise mean flow because of their non-zero streamwise permeability as shown in Table 5. The negative velocities in cases Y and YZ indicate the presence of stable recirculation vortices that do not significantly affect outer layer flows. This is considered to be similar to the sheltering effect observed in the flows over the d-type roughness (Jiménez, 2004).

The effects of the porous wall on the Reynolds normal stresses are shown in Fig. 8, which indicates profiles of the fluid-phase x–z plane-averaged Reynolds normal stresses $R_{ij}^{\mathrm{p}+} = \left[\overline{u_i' u_j'}\right]^{\mathrm{f}} / (u_\tau^{\mathrm{p}})^2$. In cases YZ, XY, and XYZ, the maximum peak values of $R_{11}^{\mathrm{p}+}$ over the porous layer are smaller than that of case Y whereas $R_{22}^{\mathrm{p}+}$ near the porous interface is substantially enhanced compared with that of case Y. The enhanced wall-normal velocity fluctuations penetrate the porous layer mainly due to the role of the pressure diffusion (Kuwata and Suga, 2016c). This trend is particularly notable in cases XY and XYZ, supporting the observation in the visualizations of Figs. 5 and 6. In contrast, the Reynolds normal stresses in case Y seems to be hardly affected by the porous surface, and the turbulence penetration into the porous layer is much smaller than that in the other cases. This is because the recirculating flows inside the pores block the intrusion of the vortex motions coming from the outer layer. Hence, it can be said that the flow characteristics over case Y are similar to those over the d-type rough wall. Note that the normalized hole size in case Y is $D_1^{\mathrm{p}+} \simeq 17$. Since the flow penetration is limited in the region of $-1 < y/D_2$ (where $D_2 = 1.3D_1$) for case Y as seen in Fig. 7(b), the scale of the "effective" surface roughness is considered to be around 22 wall units. The surface roughness effect in case Y is thus limited to the earlier stage of the transitional roughness regime. It is summarized that the porous wall with the streamwise permeability (cases XY and XYZ) gives a significant increase in the turbulent frictional drag while the wall-normal permeability itself has minor effects. Although this remark is in accordance with the results of Kuwata and Suga (2017); Suga et al. (2018), its validity may be limited to porous media with $K_{xx}/K_{yy} < 1$ since Rosti et al. (2018); Gómez-de Segura and García-Mayoral (2019) reported that the turbulence frictional drag tended to reduce when $K_{xx}/K_{yy} \gg 1$.

4.2.2. Thermal field statistics

Figures 9 and 10 show profiles of the fluid-phase x–z plane-averaged mean temperature $\varTheta_{\mathrm{f}}^{\mathrm{p}+} = \left[\bar{\theta}\right]^{\mathrm{f}}/\theta_\tau^{\mathrm{p}}$ and the root mean square of the temperature variance $\theta'^{\mathrm{p}+}_{\mathrm{f_{rms}}} = \sqrt{\left[\overline{\theta'\theta'}\right]^{\mathrm{f}}}/\theta_\tau^{\mathrm{p}}$ for the isothermal and conjugate heat transfer cases, respectively. For the conjugate heat transfer, those of the solid phase: $\varTheta_{\mathrm{s}}^{\mathrm{p}+}$ and $\theta'^{\mathrm{p}+}_{\mathrm{s_{rms}}}$, are also plotted in Fig. 10. In the clear flow region: $0 < y/H < 1$ in Figs. 9 and 10, it is seen that the difference of the thermal boundary conditions hardly affects the profiles of $\varTheta_{\mathrm{f}}^{\mathrm{p}+}$ and $\theta'^{\mathrm{p}+}_{\mathrm{f_{rms}}}$. However, the profiles in the porous layer differ by the thermal boundary condition. As shown in Fig. 9 (a), the fluid temperature for the isothermal cases becomes almost constant at $\varTheta_{\mathrm{f}} = \varTheta_{\mathrm{w}}$ inside the porous layer of $y/H < -0.2$, while $\varTheta_{\mathrm{f}}^{\mathrm{p}+}$ with the conjugate heat transfer shows almost linear profile deep inside the porous layer as seen in Fig. 10 (a). It is considered that these mean temperature profiles depend on the porosity. Indeed, the profile in case XY-C ($\varphi = 0.7$) is close to that in case YZ-C ($\varphi = 0.7$). The possible explanation for this trend is that the profile deep inside the porous layer almost reaches the equilibrium state and is similar to the laminar solution (linear profile). Accordingly, the effective thermal diffusivity $(1-\varphi)\gamma_{\rm s} + \varphi\gamma_{\rm f}$, which is expressed as a function of φ, is the factor to determine the profiles.

A comparison of the fluid- and solid-phase mean temperatures: $\mathit{\Theta}_{\rm f}^{\rm p+}$ and $\mathit{\Theta}_{\rm s}^{\rm p+}$, for the conjugate heat transfer cases shown in Fig. 10 indicates that $\mathit{\Theta}_{\rm f}^{\rm p+}$ and $\mathit{\Theta}_{\rm s}^{\rm p+}$ almost reach the equilibrium state in the porous layer while the temperature variance of the fluid phase significantly deviates from that of the solid phase except for case Y-C. The larger temperature variance of the fluid phase is due to the penetrated turbulent flow convection into the porous layer. Another important phenomenon shown in Fig. 10 (b) is that $\theta'^{\rm p+}_{\rm f_{rms}}$ in the porous layer is obviously larger in case XY-C than that in case YZ-C despite that their mean temperature profiles are nearly the same. This confirms that the streamwise permeability is more influential in increasing $\theta'^{\rm p+}_{\rm f_{rms}}$ than the spanwise permeability, which can also be confirmed in the isothermal condition although the values are significantly small in Fig. 9 (b). With the isothermal condition, the profiles of $\mathit{\Theta}_{\rm f}^{\rm p+}$ become flat at $y/D_2 < -2$ as seen in Fig. 9 (a). Since the mean temperature gradient produces temperature fluctuations, $\theta'^{\rm p+}_{\rm f_{rms}}$ vanishes at $y/D_2 < -2$ as seen in Fig. 9 (b).

Figure 10 (b) also confirms that the profiles of $\theta'^{\rm p+}_{\rm f_{rms}}$ for the conjugate heat transfer exhibit obvious peaks inside the porous layer at $-0.3 < y/H < -0.1$ for cases YZ-C, XY-C, and XYZ-C. The magnitude of the temperature variance inside the porous layer seems considerably sensitive to the porous medium geometry. Indeed, there are considerable differences in the peak values of $\theta'^{\mathrm{p}+}_{\mathrm{f_{rms}}}$ between cases XY-C and XYZ-C despite the fact that the profiles in the clear flow region are close to each other. Moreover, it is surprising that the peak value of case XYZ-C in the porous layer is larger than that in the clear flow region. Note that the significant rise in the temperature variance inside the porous layer was also observed by the DNS of turbulent heat transfer in the adiabatic/heated cube arrays by Chandesris et al. (2013) while the Prandtl number, thermal boundary conditions, and geometry of the porous medium were different from those in the present study. Chandesris et al. (2013) also reported that the large-scale temperature fluctuations in the porous medium region were caused by the combined effects of large-scale velocity fluctuations by the K–H instability and a large temperature gradient. Although the discussion on the K–H instability of the present cases is carried out in section 4.4, the visualization of Fig. 6 (b-d) indicates high- and low-temperature regions, which look much larger than the hole size which is a typical length-scale of the porous structure, and implies the existence of the K–H rollers, . Hence, it is suggested that the observed trend in Figs.10(b) is general when a large temperature gradient exists inside a porous layer.

To understand the turbulent thermal field in more detail, the x–z plane-averaged vertical turbulent heat flux $H_2^{\mathrm{t}\ \mathrm{p}+} = \left[\overline{v'\theta'}\right]^{\mathrm{f}} / (u_\tau^{\mathrm{p}}\theta_\tau^{\mathrm{p}})$, vertical temperature gradient $G_{\theta 2}^{\mathrm{p}+} = (\partial \left[\overline{\theta}\right]^{\mathrm{f}} / \partial y)/(u_\tau^{\mathrm{p}}\theta_\tau^{\mathrm{p}}/\nu)$, and the production of the temperature variance $P_\theta^{\mathrm{p}+} = -G_{\theta 2}^{\mathrm{p}+} H_2^{\mathrm{t}\ \mathrm{p}+}$ are plotted in Figs. 11 and 12. As with the temperature variance in Figs. 9 and 10, any clear difference cannot be seen in the clear channel region while difference is obvious inside the porous layer. As shown in Figs. 11 (a) and 12 (a), $H_2^{\mathrm{t}\ \mathrm{p}+}$ over the porous layer in cases Y-I and Y-C does not increase while, in the other cases, the enhancement of $H_2^{\mathrm{t\ p+}}$ over the porous layer is distinctive. In particular, over the porous media with the streamwise permeability, $H_2^{\mathrm{t\ p+}}$ is substantially enhanced corresponding to the enhancement of $R_{22}^{\mathrm{p+}}$ seen in Fig. 8. When attention is given to the porous layer region, it is found from Figs. 11 (a) and 12 (a) that $H_2^{\mathrm{t\ p+}}$ with the conjugate heat transfer condition is in a considerably higher level than that with the isothermal condition, which is similar to the trend of the temperature variance. This difference is principally due to the difference in $-G_{\theta 2}^{\mathrm{p+}}$ inside the porous layer where $-G_{\theta 2}^{\mathrm{p+}}$ with the conjugate heat transfer condition is much larger than that with the isothermal condition, resulting in the larger production $P_{\theta}^{\mathrm{p+}}$. With the conjugate heat transfer condition, the temperature gradient $-G_{\theta 2}^{\mathrm{p+}}$ in case Y-C reaches a plateau inside the porous layer of $y/H < -0.2$ while $-G_{\theta 2}^{\mathrm{p+}}$ in cases YZ-C, XY-C, and XYZ-C generally increases as it approaches the bottom wall at $y = -h$. The magnitude of the temperature gradient $-G_{\theta 2}^{\mathrm{p+}}$ in case XYZ-C is the largest, followed by that in cases XY-C and YZ-C. In cases YZ-C, XY-C, and XYZ-C, the temperature gradient $-G_{\theta 2}^{\mathrm{p+}}$ generally increases toward the bottom wall while the vertical turbulent heat flux $H_2^{\mathrm{t\ p+}}$ decreases inside the porous layer. Consequently, since $P_{\theta}^{\mathrm{p+}} = -G_{\theta 2}^{\mathrm{p+}} H_2^{\mathrm{t\ p+}}$, the profile of the production term has the local maximum point inside the porous layer around $y/H \simeq -0.2$, resulting in the rms profile of Fig. 10 (b). It should be noted that although the profile of $-G_{\theta 2}^{\mathrm{p+}}$ has kinks corresponding to the porous geometry, the local maximum point discussed above results from the general trends of $-G_{\theta 2}^{\mathrm{p+}}$ and $H_2^{\mathrm{t\ p+}}$. This suggests that the significant increase in the temperature variance inside the porous media can be a general trend that does not depend on the specific porous geometry. Indeed, the significant rise in the temperature variance inside the porous wall was observed in the DNS (Chandesris et al., 2013) in which the geometry of the porous media was totally different from those employed in the present study.

To discuss the dispersion quantities, Fig. 13 shows profiles of the x–z plane-dispersion stress $\mathcal{T}_{12}^{\mathrm{p}+} = \left[\tilde{\bar{u}}\tilde{\bar{v}}\right]^{\mathrm{f}} / (u_\tau^{\mathrm{p}})^2$ and vertical dispersion heat flux $H_2^{\mathrm{d\ p}+} = \left[\tilde{\bar{v}}\tilde{\bar{\theta}}\right]^{\mathrm{f}} / (u_\tau^{\mathrm{p}}\theta_\tau^{\mathrm{p}})$. All profiles maintain certain levels of magnitude in $-1.0 < y/D_2 < 0.0$ which corresponds to the unit cell of the porous structure. In the region of $y/D_2 < -2.0$ with the isothermal condition, $H_2^{\mathrm{d\ p}+}$ vanishes in all cases (Fig. 13(b)) while with the conjugate heat transfer condition, those in cases XY-C and XYZ-C still have non-negligible values (Fig. 13(c)). It is seen that the dispersion heat flux with the conjugate heat transfer is approximately three times larger than that of the isothermal condition, and its level of magnitude is quite comparable to that of the turbulent heat flux shown in Fig. 12(a) though the contribution of $H_2^{\mathrm{d\ p}+}$ is confined just beneath the porous interface. For the contribution to the heat transfer, what can be seen in Fig. 13 is that although the dispersion stress $\mathcal{T}_{12}$ of case YZ is much smaller in magnitude than those of cases XY and XYZ in $-1.0 < y/D_2$, the dispersion heat fluxes $H_2^{\mathrm{d\ p}+}$ of those cases have similar magnitudes for each thermal condition. This means that in cases YZ-I and YZ-C the dispersion affects heat transfer more significantly than momentum transfer.

As for the relation with the flow field, although the signs of $H_2^{\mathrm{d\ p}+}$ are positive in $y/D_2 < 0.0$ for all cases, signs of $\mathcal{T}_{12}^{\mathrm{d\ p}+}$ in cases Y and YZ are negative in $-1.0 < y/D_2 < 0.0$. This results from the mean reverse flows which were seen only in cases Y and YZ just below the porous interface as shown in Fig. 7(b). Overall, a general correlation between the dispersion stress and the dispersion heat transfer cannot be seen both in quantitative and qualitative points of view.

4.3. Quadrant analysis

In order to see the conditional events of turbulent heat transfer, as shown in Fig. 14 (a), following Katul et al. (1997) the wall-normal turbulent heat flux is decomposed into the first quadrant (Q_1): thermal ejection (hot outward flux), the second quadrant (Q_2): outward interaction, the third quadrant (Q_3): thermal sweep (cold inward flux) and the fourth quadrant (Q_4): inward interaction. Notice that the events in quadrants 1 and 3 define thermal ejections and sweeps for heat fluxes while events in quadrants 2 and 4 define ejections and sweeps for momentum fluxes as shown in Fig. 14 (b).

Figure 15 shows snapshots of the instantaneous quadrant events over the porous interfaces with the conjugate heat transfer at $y^{\mathrm{p}+} = 13$. Note that since the heat transfer characteristics over the isothermal porous layer are similar to those of the conjugate heat transfer, we focus on the latter condition. In case Y-C (Fig. 15 (a)), it is observed that all events take place along elongated streaky structures while those structures tend to be twisted and become shorter in case YZ-C (Fig. 15 (b)). The events of Q_1 thermal ejections and Q_3 thermal sweeps become dominant in this case. When the streamwise permeability exists, in case XY-C (Fig. 15 (c)), thermal ejections and sweeps form clusters aligning in the spanwise direction and those clusters become more obvious in case XYZ-C (Fig. 15 (d)) indicating the existence of transverse wavy structures. Due to the nature of the passive scalar, those trends closely relate to the trends of the structural change of the turbulent stress field observed by the previous study (Kuwata and Suga, 2017).

For the quadrant events inside the porous layers, Fig. 16 shows snapshots of the instantaneous quadrant events with the conjugate heat transfer at $y^{\mathrm{p}+} = -14$. These snapshots are taken at the same instants as those of the snapshots shown in Fig. 15. When these maps are compared with those of Fig. 15, it is obvious that generally the areas of the thermal ejections shrink and particularly in cases XY-C and XYZ-C (Fig. 16 (c, d)), the regions of the Q_1 events are partly replaced by those of Q_2. This indicates that the certain parts of the cold outward motions (Q_2) inside the porous layer receive thermal energy in the interface region and become the hot ejections (Q_1) over the porous layer. The opposite phenomenon: the certain parts of cold sweeps (Q_3) from the channel core receive thermal energy in the interface region and become the hot inward motions (Q_4) under the interface, is also recognized. However, it is seen that the shrinking areas of the thermal sweeps under the interface are not so large as those of the thermal ejections.

To discuss the statistical quadrant events, the x–z plane-averaged events of the vertical turbulent heat flux are presented in Figs. 17 and 18. The plane-averaged quadrants are defined as

$$\overline{Q_i}^{\mathrm{p}+} = \frac{1}{u_\tau^{\mathrm{p}} \theta_\tau^{\mathrm{p}} \Sigma N_i} \sum \left[v' \theta' \right]_i^{\mathrm{f}}, \tag{24}$$

where subscript i (=1–4) corresponds to the quadrant event. In cases Y-I (Fig. 17 (a)) and Y-C (Fig. 18 (a)), all quadrants events almost vanish inside the porous layer, while the overall profiles look nearly symmetric in the clear channel region regardless of the thermal boundary condition. This is because the penetration into the porous layer is significantly shorter than that of the other cases as suggested by the distributions of $H_2^{\mathrm{t}\ \mathrm{p}+}$ (Figs. 11 (a) and 12 (a)) resulting in similar distribution profiles to those of impermeable channel flows. For all cases it is clear that intensive events across the channel are $\overline{Q_1}^{\mathrm{p}+}$ and $\overline{Q_3}^{\mathrm{p}+}$. Over the porous interface, $\overline{Q_1}^{\mathrm{p}+}$ becomes larger in the order of cases Y, YZ, and XY$\simeq$XYZ while the profile of $\overline{Q_3}^{\mathrm{p}+}$ does not significantly change in cases YZ, XY, and XYZ irrespective of the thermal boundary condition. Those profiles do not show considerable difference near the top smooth wall. Inside the porous layer, the magnitude of $\overline{Q_3}^{\mathrm{p}+}$ becomes larger than that of $\overline{Q_1}^{\mathrm{p}+}$ while both $\overline{Q_1}^{\mathrm{p}+}$ and $\overline{Q_3}^{\mathrm{p}+}$ are still dominant. This trend corresponds to the event maps shown in Fig. 16 which shows larger areas of Q_3 than those of Q_1. This is because cold inward fluids receive thermal energy through the porous layer and fully heated fluids are eventually ejected to the clear channel region. In the conjugate heat transfer cases, obviously the penetration effect for case XY (Fig. 18 (c)) is more significant than that for case YZ (Fig. 18 (b)). This confirms that the streamwise permeability enhances more the penetration than the spanwise permeability. In case XYZ (Fig. 18 (d)) with both the permeabilities, the penetration effect becomes most significant.

4.4. Two-point spatial correlation

In the previous report by Kuwata and Suga (2017), the detailed discussions on the characteristic length-scale of the K–H roller (for the same porous layers as those of the present study) were carried out through the two-point spatial correlation and spectral analyses. Thus, this study focuses on the influence of the K–H roller on the temperature fluctuations by the two-point spatial correlation analysis. Figure 19 presents the streamwise spatial correlations of the streamwise velocity and temperature fluctuations at $y^{\mathrm{p}+} \simeq 13$ for the conjugate heat transfer cases. The definitions of the correlation functions are

$$R_{uu,\ x} = \frac{\overline{u'(x)u'(x+\Delta_x)}}{\overline{u'(x)u'(x)}},\ R_{\theta\theta,\ x} = \frac{\overline{\theta'(x)\theta'(x+\Delta_x)}}{\overline{\theta'(x)\theta'(x)}}. \tag{25}$$

In this discussion, a twice longer computational box of $14H(x)\times(H+h)(y)\times 3.5H(z)$ is applied to cases Y and XY since the box length of $7H$ is found not to be long enough for the two-point spatial correlation analysis. Note that as discussed in Appendix B, the turbulence statistics discussed in this study are not deteriorated by the computational box length of $7H$. In Fig. 19 (a), $R_{uu,\ x}$ in cases YZ-C, XY-C, and XYZ-C decays more rapidly than that in case Y-C. This is considered to be from the reduction of the streamwise elongated streaks (Kuwata and Suga, 2016b). In addition, the wavy profiles of $R_{uu,\ x}$ in cases XY-C and XYZ-C clearly show local minima at $\mathit{\Delta}^{\mathrm{p}+}_{x,\ \mathrm{min}} \simeq 440$ and 470, respectively. They result from the presence of the spanwise K–H rollers, and the statistical wavelengths of the K–H rollers are estimated to be $\lambda_{\mathrm{KH}}/\delta^{\mathrm{p}} = 2\mathit{\Delta}_{x,\ \mathrm{min}}/\delta^{\mathrm{p}}$ =3.7 and 3.5 for cases XY-C and XYZ-C, respectively. (These values agree with the previous results of Kuwata and Suga (2017).) Moreover, the values of $\lambda_{\mathrm{KH}}/\delta^{\mathrm{p}} = 3.5$ and 3.7 lie within the range of 3.4–5.5 that was derived by Suga et al. (2018) from a large amount of experimental and DNS data.

Similar trends can be found in the streamwise spatial correlations of the temperature fluctuations $R_{\theta\theta,\ x}$ as shown in Fig. 19 (b). In cases XY-C and XYZ-C, the profiles of $R_{\theta\theta,\ x}$ exhibit local minima at $\mathit{\Delta}^{\mathrm{p}+}_{x,\ \mathrm{min}} \simeq 400$ and 460 in cases XY-C and XYZ-C, respectively. These values agree with those of $R_{uu,\ x}$ within 10% deviations although the magnitudes of the local minima of $R_{\theta\theta,\ x}$ are smaller than those of $R_{uu,\ x}$. This observation suggests that the coherent large-scale structures in temperature fluctuations over the porous wall in cases XY-C and XYZ-C (observed in Figs. 6 and 15) are accompanied by the large-scale velocity structures induced by the K–H instability.

About the turbulent transport around the porous wall, the budget term analysis for the turbulent flow over a permeable porous layer by Kuwata and Suga (2016c) found that the increased turbulence and the greater turbulence penetration toward the porous layer were both due to the increased re-distribution and pressure diffusion processes intensified significantly by the K–H instability. It is thus worth noting that the enhanced wall-normal velocity fluctuations over the porous layer are primarily due to the enhanced pressure fluctuations induced by the K–H instability. Accordingly, it is considered that the momentum transfer at the porous interface is increased by the K–H instability, and this in tern increases heat transfer over the porous layer.

4.5. Joint probability density functions

To statistically understand the relation between the spanwise vorticity and temperature fluctuations, this section discusses the joint probability density function $p(\theta', {\omega'}_z)$ of the temperature fluctuation $\theta'/\theta'_{\mathrm{rms}}$ and the spanwise vorticity fluctuation $\omega'_z/\omega'_{z_{\mathrm{rms}}}$ at $y^{\mathrm{p}+} \simeq 13$. In Fig. 20 (a), the region of $p(\theta', {\omega'}_z) > 0.9$ (surrounded by a white border line) is located in the fourth quadrant. This suggests that high temperature fluids of $\theta' > 0$ in the porous layer are most frequently ejected by counter-clockwise vortices in case Y-C. However, in cases YZ-C, XY-C, and XYZ-C, where the effects of the porous layer on turbulence is more significant, different trends can be observed. Particularly, in cases XY-C and XYZ-C, the regions of $p(\theta', {\omega'}_z) > 0.9$ are located in the third quadrant indicating that most frequent events are counter-clockwise vortices carrying low temperature fluids toward the porous layer. Since the existence of the K–H instability is evident in cases XY-C and XYZ-C, those counter-clockwise vortices are considered to be parts of the K–H roller vortices.

4.6. Heat transfer performance

To discuss the heat transfer performance of the channel, a pumping power coefficient (normalized pumping power per unit volume) W_{p} and the Nusselt number Nu for each case are listed in Table 7 and plotted in Fig. 21. Here, W_{p} and Nu are defined as:

$$W_{\mathrm{p}} = \frac{\mathrm{d}P}{\mathrm{d}x}\frac{2}{\rho U_b^2}\int_{-h}^{H}\frac{[\bar{u}]^{\mathrm{f}}}{U_b}\mathrm{d}y, \tag{26}$$

$$\mathrm{Nu} = \frac{\overline{q_{\mathrm{w}}^{\mathrm{p}}}H}{\lambda(\Theta_{\mathrm{p}} - \Theta_0)}, \tag{27}$$

where $\overline{q_{\mathrm{w}}^{\mathrm{p}}}$, λ and Θ_{p} are the averaged heat flux on the porous interface, the thermal conductivity of the fluid and the mean temperature of the porous interface, respectively. A plane-channel flow at the bulk Reynolds number of 2900 is also simulated for the comparison. It can be seen that $W_{\mathrm{p}}/W_{\mathrm{PCH}}$ in case Y is about 1.02 while in case YZ, it is about 1.55, where W_{PCH} is the pumping power coefficient of the plane channel case. In cases XY and XYZ, W_{p} are 2.2 and 2.5 times larger than that of the plane channel W_{PCH}, respectively. This trend corresponds to the previously reported results that the Reynolds shear stresses were more increased over the porous wall with spanwise and streamwise permeabilities than that near the smooth top wall and the streamwise permeability enhances more turbulence than the spanwise permeability (Kuwata and Suga, 2017).

In Fig. 21 (b), the Nusselt numbers in the isothermal cases are all larger than that in the smooth wall case. Compared with the plane channel case, the increase rate of Nu is 36% in case YZ-I while the porous wall with the streamwise permeability considerably increases Nu by factors of 1.82 (case XY-I) and 1.97 (case XYZ-I). Because the surface turbulence characteristics are similar to those of the isothermal cases (as discussed in section 4.2), for the Nusselt numbers of the conjugate heat transfer with the spanwise permeability, the increase rate of Nu to the plane channel case is 38% in case YZ-C while the porous wall with the streamwise permeability increases Nu by factors of 1.87 (case XY-C) and 2.01 (case XYZ-C). Supporting this trend, Fig. 12(a) indicates that the levels of turbulent heat flux inside the porous layers in cases XY-C and XYZ-C are larger than that in case YZ-C. Consequently, it is confirmed that the contribution of the streamwise permeability is more efficient than that of the spanwise permeability with respect to the heat transfer performance of the channel. Note that although the conjugate heat transfer cases show slightly better heat transfer performance (in cases YZ, XY and XYZ), it is difficult to compare the performance in the different boundary conditions since the Nusselt numbers significantly depend on the definition of the representative temperature difference.

Finally, Fig. 22 (a) shows the dependency of W_p and Nu on the permeability Reynolds number Re_K. It is clearly seen that W_p and Nu increase as Re_K increases although the correlations are not linear. However, when the surrogate permeability Reynolds number, which was introduced by Suga et al. (2018) as

$$\mathrm{Re}_K^{**} = c\frac{u_\tau^\mathrm{p} D_{\mathrm{p}_x}}{\nu}, \tag{28}$$

with the given coefficient $c = 1/3.8$, is applied, the distributions become nearly linear as shown in Fig. 22 (b). Here, the streamwise pore size D_{p_x} corresponds to D_1 in this study. Since D_1 is constant, the profiles of Fig. 22 (b) simply show that those parameters simply depend on the friction velocity irrespective of the case difference. In other words, the characteristic length scale for the surface turbulence and turbulent heat transfer of the present porous media does not significantly change although the porous structures are very different. This suggests an important idea for the discussion on the characteristic length scale.

5. Concluding remarks

To investigate the effects of the anisotropic wall permeability on turbulent thermal field in forced convection porous-walled channel flows, direct numerical simulations are performed by the lattice Boltzmann method. The considered bulk flow Reynolds number is 2900. The surfaces of the fully resolved porous structures are treated with isothermal and conjugate heat transfer conditions. The following list summarizes the remarks obtained in this study.

(1) In the case of $K_{xx}/K_{yy} < 1$, the wall-normal permeability itself has minor effects on the turbulent thermal field over and inside porous media. However, the streamwise permeability significantly enhances the thermal turbulence and its effect is stronger than that of the spanwise permeability. These trends result from the flow field turbulence.

(2) Although the velocities deeply penetrate into the porous wall in cases with both wall-normal and streamwise permeabilities by the K–H insta-

bility, the temperatures do not penetrate so deeply with the isothermal wall boundary condition. With the conjugate heat transfer the temperature penetration becomes as deep as that of the velocity leading to a large mean temperature gradient. This is because the changes of the fluid temperatures immediately affect the porous wall temperatures by the conjugate heat transfer and thus the significance of temperature fluctuations tends to be maintained deeply in the porous layer. Accordingly, with the the conjugate heat transfer, temperature fluctuations inside the porous layers become as large as those outside the porous layers.

(3) The dispersion heat flux with the conjugate heat transfer is approximately three times larger than that of the isothermal condition, and it is comparatively as large as the turbulent heat flux under the interface. The general correlation between the dispersion stress and heat flux terms cannot be seen.

(4) Just below the interface the thermal sweeps are most dominant while the thermal ejections overtake them over the porous layer. This is because cold inward fluids receive thermal energy through the porous layer and fully heated fluids are eventually ejected to the clear channel region.

(5) Pumping power and turbulent heat transfer over porous walls significantly increases as the permeability Reynolds number increases. It is then confirmed that the contribution of the streamwise permeability is more efficient than that of the spanwise permeability with respect to the heat transfer performance of the channel.

Acknowledgements

The numerical simulations were carried out by TSUBAME3.0 supercomputer in Tokyo Institute of Technology, Japan in the research project: hp180023 supported by the High Performance Computing Infrastructure (HPCI) of the Research Organization for Information Science and Technology (RiST), Japan.

Appendix A. The imbalance-correction (IBC) zonal grid refinement method for thermal fields

For simplicity, a two dimensional case is applied to describe the numerical procedure. For the imbalance-correction zonal grid refinement method, a face-to-face grid system is considered as illustrated in Fig. 23, which shows the distribution functions at the coarse and fine grids. They are transferred to another grid on the boundary line A. Here, the superscripts "c" and "f" denote values at the coarse and fine grids, respectively. The dashed arrows mean the distribution functions which are transferred from the coarse to fine grids and from the fine to coarse grids (indicated by the superscripts "c→f" and "f→c", respectively).

In the thermal field, considering the energy conservation at the grid boundary nodes between the coarse and fine grids, an energy imbalance $\mathcal{E}_\theta$ can be evaluated as

$$\mathcal{E}_\theta = \sum_{\beta_\mathrm{c}} g_{\beta_\mathrm{c}}^{\mathrm{neq,\ c}} + \sum_{\hat{\beta}_\mathrm{c}} g_{\hat{\beta}_\mathrm{c}}^{\mathrm{neq,\ f\to c}} = n \frac{\tau^\mathrm{c}}{\tau^\mathrm{f}} \left(\sum_{\hat{\beta}_\mathrm{c}} g_{\hat{\beta}_\mathrm{c}}^{\mathrm{neq,\ f}} + \sum_{\beta_\mathrm{c}} \tilde{g}_{\beta_\mathrm{c}}^{\mathrm{neq,\ c\to f}} \right), \qquad (29)$$

where the subscripts β_c and $\hat{\beta}_\mathrm{c}$ indicate known and unknown directions of the distribution functions at the coarse grid boundary, respectively. The notation

"$\sim$" means the spatially and temporally interpolated distribution function, which is required to compensate the differences of the lattice spacing and the time step between the coarse and fine grids. The relations of the lattice spacing and the time step between the coarse and fine grids are defined respectively as: $\mathit{\Delta}^{\mathrm{c}} = n\mathit{\Delta}^{\mathrm{f}}$ and $\delta t^{\mathrm{c}} = n\delta t^{\mathrm{f}}$, where n is the grid refinement ratio. The macroscopic interface variable θ is corrected using the imbalance $\mathcal{E}_\theta$ with a weighting factor λ_θ as

$$\check{\theta} = \theta + \lambda_\theta \mathcal{E}_\theta. \tag{30}$$

Following the same procedure for the momentum by Kuwata and Suga (2016a), the weighting factor can be estimated as

$$\lambda_\theta = \left\{ 1 - \frac{1}{6}\left(1 - n\frac{\tau_{\mathrm{c}}}{\tau_{\mathrm{f}}}\right)\left(1 + \frac{c^2}{c_{\mathrm{s}}^2}\frac{u_x}{c}\right)\right\}^{-1}, \tag{31}$$

where $c = \mathit{\Delta}^{\mathrm{c}}/\delta t^{\mathrm{c}}$ and u_x denotes the velocity in the vertical direction to the grid boundary face.

Appendix B. Influence of the computational domain size

Figure 24 compares the profiles of $R_{uu,\ x}$ by the simulations with two computational boxes of $7H(x) \times (H + h)(y) \times 3.5H(z)$ and $14H(x) \times (H + h)(y) \times 3.5H(z)$. In case XY, the locations and values of the minima are not significantly different between the two results while the larger box simulation yields a much faster decay profile. It is also confirmed that $R_{uu,\ x}$ in case Y with the larger box simulation decays to zero at $\mathit{\Delta}_x^{\mathrm{p}+} \simeq 1200$. Although it is not shown here, the trend of $R_{\theta\theta,\ x}$ is the same as that of $R_{uu,\ x}$. To assess the influence of those computational domain sizes on the turbulence statistics, Fig. 25 compares the second-order turbulence statistics obtained with those boxes. It is obvious that there is no perceptible difference in the streamwise Reynolds stress (Fig. 25 (a)) and temperature variance (Fig. 25 (b)). Correspondingly, it can be said that the computational domain of $7H(x) \times (H+h)(y) \times 3.5H(z)$ does not deteriorate the turbulence statistics discussed in this study.

References

Bespalko, D., Pollard, A., Uddin, M., 2012. Analysis of the pressure fluctuations from an LBM simulation of turbulent channel flow. Comput. Fluids 54, 143–146.

Breugem, W.P., Boersma, B.J., 2005. Direct numerical simulations of turbulent flow over a permeable wall using a direct and a continuum approach. Phys. Fluids 17, 025103.

Breugem, W.P., Boersma, B.J., Uittenbogaard, R.E., 2006. The influence of wall permeability on turbulent channel flow. J. Fluid Mech. 562, 35–72.

Chandesris, M., D'Hueppe, A., Mathieu, B., Jamet, D., Goyeau, B., 2013. Direct numerical simulation of turbulent heat transfer in a fluid-porous domain. Phys. Fluids 25, 125110.

Detert, M., Nikora, V., Jirka, G.H., 2010. Synoptic velocity and pressure fields at the water-sediment interface of streambeds. J. Fluid Mech. 660, 55–86.

Drazin, P., Howard, L., 1966. Hydrodynamic stability of parallel flow of inviscid fluid, Elsevier. volume 9 of *Adv. Appl. Mech.*, pp. 1 – 89.

Finnigan, J., 2000. Turbulence in plant canopies. Ann. Rev. Fluid Mech. 32, 519–571.

He, X., Chen, S., Doolen, G.D., 1998. A novel thermal model for the lattice Boltzmann method in incompressible limit. J. Comput. Phys. 146, 282–300.

He, X., Luo, L.S., 1997. Lattice Boltzmann model for the incompressible Navier–Stokes equation. J. Stats. Phys. 88, 927–944.

Ho, R.T., Gelhar, L.W., 1973. Turbulent flow with wavy permeable boundaries. J. Fluid Mech. 58, 403–414.

Jiménez, J., 2004. Turbulent flows over rough walls. Annu. Rev. Fluid Mech. 36, 173–196.

Katul, G., Kuhn, G., Scheildge, J., Hsieh, C.I., 1997. The ejection-sweep character of scalar fluxes in the unstable surface layer. Boundary-Layer Meteorol. 83, 1–26.

Kim, J., Moin, P., Moser, R., 1987. Turbulence statistics in fully developed channel flow at low Reynolds number. J. Fluid Mech. 177, 133–166.

Kong, F.Y., Schetz, J.A., 1982. Turbulent boundary layer over porous surfaces with different surface geometries. Technical Report 82-0030. AIAA.

Kuwata, Y., Suga, K., 2016a. Imbalance-correction grid-refinement method for lattice Boltzmann flow simulations. J. Comput. Phys. 311, 348–362.

Kuwata, Y., Suga, K., 2016b. Lattice Boltzmann direct numerical simulation of interface turbulence over porous and rough walls. Int. J. Heat Fluid Flow 61, 145–157.

Kuwata, Y., Suga, K., 2016c. Transport mechanism of interface turbulence over porous and rough walls. Flow Turb.Combust. 97, 1071–1093.

Kuwata, Y., Suga, K., 2017. Direct numerical simulation of turbulence over anisotropic porous media. J. Fluid Mech. 831, 41–71.

Latt, J., Chopard, B., 2006. Lattice Boltzmann method with regularized pre-collision distribution functions. Math. Comput. Simul. 72, 165–168.

Lovera, F., Kennedy, J.F., 1969. Friction factors for flat bed flows in sand channels. J. Hydr. Div., ASCE 95, 1227–1234.

Manes, C., Poggi, D., Ridol, L., 2011. Turbulent boundary layers over permeable walls: scaling and near-wall structure. J. Fluid Mech. 687, 141–170.

Manes, C., Pokrajac, D., McEwan, I., Nikora, V., 2009. Turbulence structure of open channel flows over permeable and impermeable beds: A comparative study. Phys. Fluids 21, 125109.

Ochoa-Tapia, A.J., Whitaker, S., 1995. Momentum transfer at the boundary between a porous medium and a homogeneous fluid. I.: Theoretical development. Int. J. Heat Mass Transfer 38, 2635–2646.

Pokrajac, D., Manes, C., 2009. Velocity measurements of a free-surface turbulent flow penetrating a porous medium composed of uniform-size spheres. Transp. Porous, Med. 78, 367–383.

Raupach, M.R., Antonia, R.A., Rajagopalan, S., 1991. Rough-wall turbulent boundary layers. Appl. Mech. Rev. 44, 1–25.

Rosti, M.E., Brandt, L., Pinelli, A., 2018. Turbulent channel flow over an anisotropic porous wall – drag increase and reduction. J. Fluid Mech. 842, 381–394.

Rosti, M.E., Cortelezzi, L., Quadrio, M., 2015. Direct numerical simulation of turbulent channel flow over porous walls. J. Fluid Mech. 784, 396–442.

Ruff, J.F., Gelhar, L.W., 1972. Turbulent shear flow in porous boundary. J. Eng. Mech. Div., ASCE 98, 975–991.

Gómez-de Segura, G., García-Mayoral, R., 2019. Turbulent drag reduction by anisotropic permeable substrates – analysis and direct numerical simulations. J. Fluid Mech. 875, 124–172.

Shimizu, Y., Tsujimoto, T., Nakagawa, H., 1990. Experiment and macroscopic modelling of flow in highly permeable porous medium under free-surface flow. J. Hydrosci. Hydraul. Eng. 8, 69–78.

Suga, K., 2016. Understanding and modelling turbulence over and inside porous media. Flow Turb. Combust. 96, 717–756.

Suga, K., Chikasue, R., Kuwata, Y., 2017a. Modelling turbulent and dispersion heat fluxes in turbulent porous medium flows using the resolved LES data. Int. J. Heat Fluid Flow 68, 225–236.

Suga, K., Kuwata, Y., Takashima, K., Chikasue, R., 2015. A D3Q27 multiple-relaxation-time lattice Boltzmann method for turbulent flows. Comput. Math. App. 69, 518–529.

Suga, K., Matsumura, Y., Ashitaka, Y., Tominaga, S., Kaneda, M., 2010. Effects of wall permeability on turbulence. Int. J. Heat Fluid Flow 31, 974–984.

Suga, K., Mori, M., Kaneda, M., 2011. Vortex structure of turbulence over permeable walls. Int. J. Heat Fluid Flow 32, 586–595.

Suga, K., Nakagawa, Y., Kaneda, M., 2017b. Spanwise turbulence structure over permeable walls. J. Fluid Mech. 822, 186–201.

Suga, K., Okazaki, Y., Ho, U., Kuwata, Y., 2018. Anisotropic wall permeability effects on turbulent channel flows. J. Fluid Mech. 855, 983–1016.

Suga, K., Tominaga, S., Mori, M., Kaneda, M., 2013. Turbulence characteristics in flows over solid and porous square ribs mounted on porous walls. Flow Turb. Combust. 91, 19–40.

Wang, J., Wang, M., Li, Z., 2007. A lattice Boltzmann algorithm for fluid-solid conjugate heat transfer. Int. J. Therm. Sci. 46, 228–234.

Whitaker, S., 1986. Flow in porous media I: A theoretical derivation of Darcy's law. Transp. Porous Med. 1, 3–25.

Whitaker, S., 1996. The Forchheimer equation: A theoretical development. Transp. Porous Med. 25, 27–61.

White, B.L., Nepf, H.M., 2007. Shear instability and coherent structures in shallow flow adjacent to a porous layer. J. Fluid Mech. 593, 1–32.

Yoshida, H., Nagaoka, M., 2010. Multiple-relaxation-time lattice Boltzmann model for the convection and anisotropic diffusion equation. J. Comput. Phys. 229, 7774–7795.

Zagni, A.F.E., Smith, K.V.H., 1976. Channel flow over permeable beds of graded spheres. J. Hydraul. Div. 102, 207–222.

Zippe, H.J., Graf, W.H., 1983. Turbulent boundary-layer flow over permeable and non-permeable rough surfaces. J. Hydraul. Res. 21, 51–65.

Table 1: Parameters of the D3Q27 discrete velocity model.

c_s/c	$\boldsymbol{\xi}_\alpha/c$	w_α
$1/\sqrt{3}$	$(0,0,0)$	$8/27$ $(\alpha=0)$
	$(\pm1,0,0),(0,\pm1,0),(0,0,\pm1)$	$2/27$ $(\alpha=1,\dots,6)$
	$(\pm1,\pm1,0),(\pm1,0,\pm1),(0,\pm1,\pm1)$	$1/54$ $(\alpha=7,\dots,18)$
	$(\pm1,\pm1,\pm1)$	$1/216$ $(\alpha=19,\dots,26)$

Table 2: Equilibrium moments.

m_0^{eq}	$= \rho$	$\equiv \sum_{\alpha=0}^{26} f_\alpha^{\mathrm{eq}}$	m_{13}^{eq}	$= \psi_x$	$\equiv \frac{9}{2} \sum_{\alpha=0}^{26} \left(\xi_{\alpha x}^2 + \xi_{\alpha y}^2 + \xi_{\alpha z}^2\right)^2 \xi_{\alpha x} f_\alpha^{\mathrm{eq}}$
m_1^{eq}	$= j_x$	$\equiv \sum_{\alpha=0}^{26} f_\alpha^{\mathrm{eq}} \xi_{\alpha x}$	m_{14}^{eq}	$= \psi_y$	$\equiv \frac{9}{2} \sum_{\alpha=0}^{26} \left(\xi_{\alpha x}^2 + \xi_{\alpha y}^2 + \xi_{\alpha z}^2\right)^2 \xi_{\alpha y} f_\alpha^{\mathrm{eq}}$
m_2^{eq}	$= j_y$	$\equiv \sum_{\alpha=0}^{26} f_\alpha^{\mathrm{eq}} \xi_{\alpha y}$	m_{15}^{eq}	$= \psi_z$	$\equiv \frac{9}{2} \sum_{\alpha=0}^{26} \left(\xi_{\alpha x}^2 + \xi_{\alpha y}^2 + \xi_{\alpha z}^2\right)^2 \xi_{\alpha z} f_\alpha^{\mathrm{eq}}$
m_3^{eq}	$= j_z$	$\equiv \sum_{\alpha=0}^{26} f_\alpha^{\mathrm{eq}} \xi_{\alpha z}$	m_{16}^{eq}	$= \varepsilon$	$\equiv \frac{3}{2} \sum_{\alpha=0}^{26} \left(\xi_{\alpha x}^2 + \xi_{\alpha y}^2 + \xi_{\alpha z}^2\right)^2 f_\alpha^{\mathrm{eq}}$
m_4^{eq}	$= e$	$\equiv \sum_{\alpha=0}^{26} \left(\xi_{\alpha x}^2 + \xi_{\alpha y}^2 + \xi_{\alpha z}^2\right) f_\alpha^{\mathrm{eq}}$	m_{17}^{eq}	$= e_3$	$\equiv \frac{9}{2} \sum_{\alpha=0}^{26} \left(\xi_{\alpha x}^2 + \xi_{\alpha y}^2 + \xi_{\alpha z}^2\right)^3 f_\alpha^{\mathrm{eq}}$
m_5^{eq}	$= XX$	$\equiv \sum_{\alpha=0}^{26} \left(2\xi_{\alpha x}^2 - \xi_{\alpha y}^2 - \xi_{\alpha z}^2\right) f_\alpha^{\mathrm{eq}}$	m_{18}^{eq}	$= XX_e$	$\equiv 3 \sum_{\alpha=0}^{26} \left(2\xi_{\alpha x}^2 - \xi_{\alpha y}^2 - \xi_{\alpha z}^2\right) \left(\xi_{\alpha x}^2 + \xi_{\alpha y}^2 + \xi_{\alpha z}^2\right) f_\alpha^{\mathrm{eq}}$
m_6^{eq}	$= WW$	$\equiv \sum_{\alpha=0}^{26} \left(\xi_{\alpha y}^2 - \xi_{\alpha z}^2\right) f_\alpha^{\mathrm{eq}}$	m_{19}^{eq}	$= WW_e$	$\equiv 3 \sum_{\alpha=0}^{26} \left(\xi_{\alpha y}^2 - \xi_{\alpha z}^2\right) \left(\xi_{\alpha x}^2 + \xi_{\alpha y}^2 + \xi_{\alpha z}^2\right) f_\alpha^{\mathrm{eq}}$
m_7^{eq}	$= XY$	$\equiv \sum_{\alpha=0}^{26} \left(\xi_{\alpha x}\xi_{\alpha y}\right) f_\alpha^{\mathrm{eq}}$	m_{20}^{eq}	$= XY_e$	$\equiv 3 \sum_{\alpha=0}^{26} \left(\xi_{\alpha x}\xi_{\alpha y}\right) \left(\xi_{\alpha x}^2 + \xi_{\alpha y}^2 + \xi_{\alpha z}^2\right) f_\alpha^{\mathrm{eq}}$
m_8^{eq}	$= YZ$	$\equiv \sum_{\alpha=0}^{26} \left(\xi_{\alpha y}\xi_{\alpha z}\right) f_\alpha^{\mathrm{eq}}$	m_{21}^{eq}	$= YZ_e$	$\equiv 3 \sum_{\alpha=0}^{26} \left(\xi_{\alpha y}\xi_{\alpha z}\right) \left(\xi_{\alpha x}^2 + \xi_{\alpha y}^2 + \xi_{\alpha z}^2\right) f_\alpha^{\mathrm{eq}}$
m_9^{eq}	$= ZX$	$\equiv \sum_{\alpha=0}^{26} \left(\xi_{\alpha z}\xi_{\alpha x}\right) f_\alpha^{\mathrm{eq}}$	m_{22}^{eq}	$= ZX_e$	$\equiv 3 \sum_{\alpha=0}^{26} \left(\xi_{\alpha z}\xi_{\alpha x}\right) \left(\xi_{\alpha x}^2 + \xi_{\alpha y}^2 + \xi_{\alpha z}^2\right) f_\alpha^{\mathrm{eq}}$
m_{10}^{eq}	$= \varphi_x$	$\equiv 3 \sum_{\alpha=0}^{26} \left(\xi_{\alpha x}^2 + \xi_{\alpha y}^2 + \xi_{\alpha z}^2\right) \xi_{\alpha x} f_\alpha^{\mathrm{eq}}$	m_{23}^{eq}	$= \tau_x$	$\equiv \sum_{\alpha=0}^{26} \xi_{\alpha x} \left(\xi_{\alpha y}^2 - \xi_{\alpha z}^2\right) f_\alpha^{\mathrm{eq}}$
m_{11}^{eq}	$= \varphi_y$	$\equiv 3 \sum_{\alpha=0}^{26} \left(\xi_{\alpha x}^2 + \xi_{\alpha y}^2 + \xi_{\alpha z}^2\right) \xi_{\alpha y} f_\alpha^{\mathrm{eq}}$	m_{24}^{eq}	$= \tau_y$	$\equiv \sum_{\alpha=0}^{26} \xi_{\alpha y} \left(\xi_{\alpha z}^2 - \xi_{\alpha x}^2\right) f_\alpha^{\mathrm{eq}}$
m_{12}^{eq}	$= \varphi_z$	$\equiv 3 \sum_{\alpha=0}^{26} \left(\xi_{\alpha x}^2 + \xi_{\alpha y}^2 + \xi_{\alpha z}^2\right) \xi_{\alpha z} f_\alpha^{\mathrm{eq}}$	m_{25}^{eq}	$= \tau_z$	$\equiv \sum_{\alpha=0}^{26} \xi_{\alpha z} \left(\xi_{\alpha x}^2 - \xi_{\alpha y}^2\right) f_\alpha^{\mathrm{eq}}$
			m_{26}^{eq}	$= XYZ$	$\equiv \sum_{\alpha=0}^{26} \left(\xi_{\alpha x}\xi_{\alpha y}\xi_{\alpha z}\right) f_\alpha^{\mathrm{eq}}$

ρ: density, $j_x,\ j_y,\ j_z$: momentum, e: kinetic energy, $XX,\ WW,\ XY,\ YZ,\ ZX$: second-order tensors, $\varphi_x,\ \varphi_y,\ \varphi_z$: flux of the energy, $\psi_x,\ \psi_y,\ \psi_z$: flux of the square of the energy, ε: square of the energy, e_3: cube of the energy, $XX_e,\ WW_e$: product of XX and WW by the energy, $XY_e,\ YZ_e,\ ZX_e$: extra-diagonal second-order moments of the energy, $\tau_x,\ \tau_y,\ \tau_z$: third-order pseudo vector, XYZ: third-order totally antisymmetric tensor.

Table 3: 27 × 27 transformation matrix.

$$\boldsymbol{M} = \begin{pmatrix}
1 & 1 & 1 & 1 & 1 & 1 & 1 & 1 & 1 & 1 & 1 & 1 & 1 & 1 & 1 & 1 & 1 & 1 & 1 & 1 & 1 & 1 & 1 & 1 & 1 & 1 & 1 \\
0 & 1 & 0 & -1 & 0 & 0 & 0 & 1 & -1 & -1 & 1 & 1 & 0 & -1 & 0 & 1 & 0 & -1 & 0 & 1 & -1 & -1 & 1 & 1 & -1 & -1 & 1 \\
0 & 0 & 1 & 0 & -1 & 0 & 0 & 1 & 1 & -1 & -1 & 0 & 1 & 0 & -1 & 0 & 1 & 0 & -1 & 1 & 1 & -1 & -1 & 1 & 1 & -1 & -1 \\
0 & 0 & 0 & 0 & 0 & 1 & -1 & 0 & 0 & 0 & 0 & 1 & 1 & 1 & 1 & -1 & -1 & -1 & -1 & 1 & 1 & 1 & 1 & -1 & -1 & -1 & -1 \\
-2 & -1 & -1 & -1 & -1 & -1 & -1 & 0 & 0 & 0 & 0 & 0 & 0 & 0 & 0 & 0 & 0 & 0 & 0 & 1 & 1 & 1 & 1 & 1 & 1 & 1 & 1 \\
0 & 2 & -1 & 2 & -1 & -1 & -1 & 1 & 1 & 1 & 1 & 1 & -2 & 1 & -2 & 1 & -2 & 1 & -2 & 0 & 0 & 0 & 0 & 0 & 0 & 0 & 0 \\
0 & 0 & 1 & 0 & 1 & -1 & -1 & 1 & 1 & 1 & 1 & -1 & 0 & -1 & 0 & -1 & 0 & -1 & 0 & 0 & 0 & 0 & 0 & 0 & 0 & 0 & 0 \\
0 & 0 & 0 & 0 & 0 & 0 & 0 & 1 & -1 & 1 & -1 & 0 & 0 & 0 & 0 & 0 & 0 & 0 & 0 & 1 & -1 & 1 & -1 & 1 & -1 & 1 & -1 \\
0 & 0 & 0 & 0 & 0 & 0 & 0 & 0 & 0 & 0 & 0 & 0 & 1 & 0 & -1 & 0 & -1 & 0 & 1 & 1 & 1 & -1 & -1 & -1 & -1 & 1 & 1 \\
0 & 0 & 0 & 0 & 0 & 0 & 0 & 0 & 0 & 0 & 0 & 1 & 0 & -1 & 0 & -1 & 0 & 1 & 0 & 1 & -1 & -1 & 1 & -1 & 1 & 1 & -1 \\
0 & -4 & 0 & 4 & 0 & 0 & 0 & -1 & 1 & 1 & -1 & -1 & 0 & 1 & 0 & -1 & 0 & 1 & 0 & 2 & -2 & -2 & 2 & 2 & -2 & -2 & 2 \\
0 & 0 & -4 & 0 & 4 & 0 & 0 & -1 & -1 & 1 & 1 & 0 & -1 & 0 & 1 & 0 & -1 & 0 & 1 & 2 & 2 & -2 & -2 & 2 & 2 & -2 & -2 \\
0 & 0 & 0 & 0 & 0 & -4 & 4 & 0 & 0 & 0 & 0 & -1 & -1 & -1 & -1 & 1 & 1 & 1 & 1 & 2 & 2 & 2 & 2 & -2 & -2 & -2 & -2 \\
0 & 4 & 0 & -4 & 0 & 0 & 0 & -2 & 2 & 2 & -2 & -2 & 0 & 2 & 0 & -2 & 0 & 2 & 0 & 1 & -1 & -1 & 1 & 1 & -1 & -1 & 1 \\
0 & 0 & 4 & 0 & -4 & 0 & 0 & -2 & -2 & 2 & 2 & 0 & -2 & 0 & 2 & 0 & -2 & 0 & 2 & 1 & 1 & -1 & -1 & 1 & 1 & -1 & -1 \\
0 & 0 & 0 & 0 & 0 & 4 & -4 & 0 & 0 & 0 & 0 & -2 & -2 & -2 & -2 & 2 & 2 & 2 & 2 & 1 & 1 & 1 & 1 & -1 & -1 & -1 & -1 \\
4 & 0 & 0 & 0 & 0 & 0 & 0 & -1 & -1 & -1 & -1 & -1 & -1 & -1 & -1 & -1 & -1 & -1 & -1 & 1 & 1 & 1 & 1 & 1 & 1 & 1 & 1 \\
-8 & 4 & 4 & 4 & 4 & 4 & 4 & -2 & -2 & -2 & -2 & -2 & -2 & -2 & -2 & -2 & -2 & -2 & -2 & 1 & 1 & 1 & 1 & 1 & 1 & 1 & 1 \\
0 & -4 & 2 & -4 & 2 & 2 & 2 & 1 & 1 & 1 & 1 & 1 & -2 & 1 & -2 & 1 & -2 & 1 & -2 & 0 & 0 & 0 & 0 & 0 & 0 & 0 & 0 \\
0 & 0 & -2 & 0 & -2 & 2 & 2 & 1 & 1 & 1 & 1 & -1 & 0 & -1 & 0 & -1 & 0 & -1 & 0 & 0 & 0 & 0 & 0 & 0 & 0 & 0 & 0 \\
0 & 0 & 0 & 0 & 0 & 0 & 0 & -2 & 2 & -2 & 2 & 0 & 0 & 0 & 0 & 0 & 0 & 0 & 0 & 1 & -1 & 1 & -1 & 1 & -1 & 1 & -1 \\
0 & 0 & 0 & 0 & 0 & 0 & 0 & 0 & 0 & 0 & 0 & 0 & -2 & 0 & 2 & 0 & 2 & 0 & -2 & 1 & 1 & -1 & -1 & -1 & -1 & 1 & 1 \\
0 & 0 & 0 & 0 & 0 & 0 & 0 & 0 & 0 & 0 & 0 & -2 & 0 & 2 & 0 & 2 & 0 & -2 & 0 & 1 & -1 & -1 & 1 & -1 & 1 & 1 & -1 \\
0 & 0 & 0 & 0 & 0 & 0 & 0 & 1 & -1 & -1 & 1 & -1 & 0 & 1 & 0 & -1 & 0 & 1 & 0 & 0 & 0 & 0 & 0 & 0 & 0 & 0 & 0 \\
0 & 0 & 0 & 0 & 0 & 0 & 0 & -1 & -1 & 1 & 1 & 0 & 1 & 0 & -1 & 0 & 1 & 0 & -1 & 0 & 0 & 0 & 0 & 0 & 0 & 0 & 0 \\
0 & 0 & 0 & 0 & 0 & 0 & 0 & 0 & 0 & 0 & 0 & 1 & -1 & 1 & -1 & -1 & 1 & -1 & 1 & 0 & 0 & 0 & 0 & 0 & 0 & 0 & 0 \\
0 & 0 & 0 & 0 & 0 & 0 & 0 & 0 & 0 & 0 & 0 & 0 & 0 & 0 & 0 & 0 & 0 & 0 & 0 & 1 & -1 & 1 & -1 & -1 & 1 & -1 & 1
\end{pmatrix}$$

Table 4: Parameters of the D3Q19 discrete velocity model.

c_s/c	$\boldsymbol{\xi}_\alpha/c$	w_α
$1/\sqrt{3}$	$(0,0,0)$	$1/3(\alpha=0)$
	$(\pm1,0,0),(0,\pm1,0),(0,0,\pm1)$	$1/18(\alpha=1,\ldots,6)$
	$(\pm1,\pm1,0),(\pm1,0,\pm1),(0,\pm1,\pm1)$	$1/36(\alpha=7,\ldots,18)$

Table 5: Parameters of computational geometry.

Case	φ	K_{xx}/H^2	K_{yy}/H^2	K_{zz}/H^2	$\varDelta^{\mathrm{c,t}+}$	$\varDelta^{\mathrm{f,p}+}$	$D_1/\varDelta^\mathrm{f}$
Y	0.56	0	3.48×10^{-4}	0	1.72	0.89	30
YZ	0.70	0	4.65×10^{-4}	4.65×10^{-4}	1.83	1.23	30
XY	0.70	4.65×10^{-4}	4.65×10^{-4}	0	1.95	1.50	30
XYZ	0.84	5.71×10^{-4}	5.71×10^{-4}	5.71×10^{-4}	2.01	1.64	30

Table 6: Reynolds numbers of the simulations.

Case	Re_b	$\mathrm{Re}_\tau^\mathrm{p}$	$\mathrm{Re}_\tau^\mathrm{t}$	Re_K
Y	2863	105	94.6	2.18
YZ	2921	180	75.0	4.94
XY	2904	240	65.9	6.00
XYZ	2891	270	62.6	8.90

Table 7: Pumping power coefficient and Nusselt numbers.

Case	$W_{\mathrm{p}}(\times 10^2)$	Nu (isothermal)	Nu (conjugate)
CH	1.86	3.42	—
Y	1.90	3.59	3.53
YZ	2.89	4.66	4.74
XY	4.03	6.25	6.39
XYZ	4.66	6.75	6.91

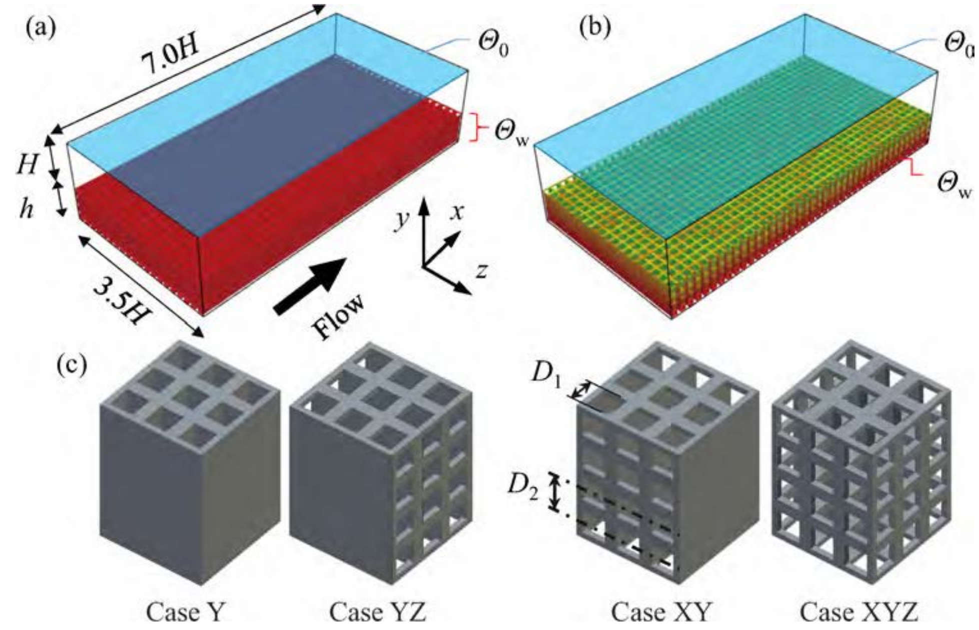
(a)
7.0H
Θ_0
Θ_w
H
h
3.5H
Flow
y
x
z
(b)
Θ_0
Θ_w
(c)
D_1
D_2
Case Y
Case YZ
Case XY
Case XYZ

Figure 1: Computational domain and geometry of the channel: (a) isothermal and (b) conjugate wall heat transfer conditions and (c) porous media: cases Y, YZ, XY, and XYZ.

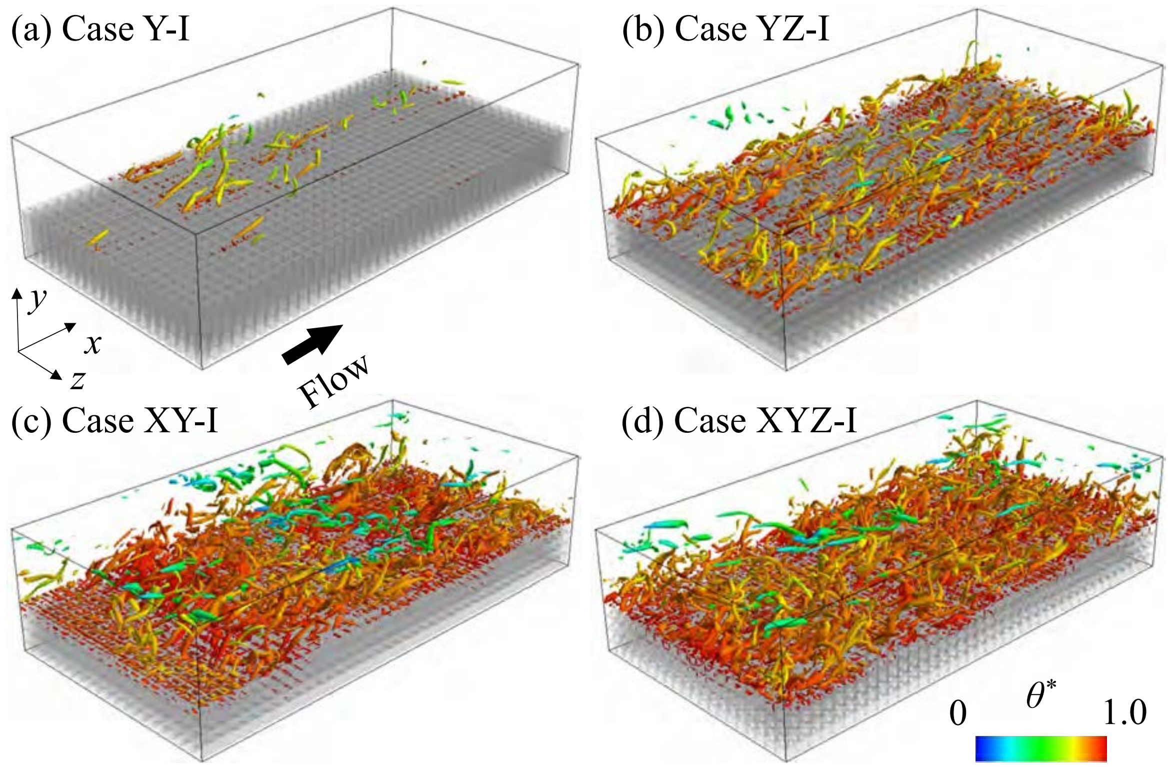
(a) Case Y-I
(b) Case YZ-I
y
x
z
Flow
(c) Case XY-I
(d) Case XYZ-I
0
θ^*
1.0

Figure 2: Snapshot of iso-surfaces of the second invariant of the velocity gradient tensor $II^* = 15$ colored by the local instantaneous temperatures $0 < \theta^* < 1.0$: (a) case Y-I, (b) case YZ-I, (c) case XY-I, and (d) case XYZ-I.

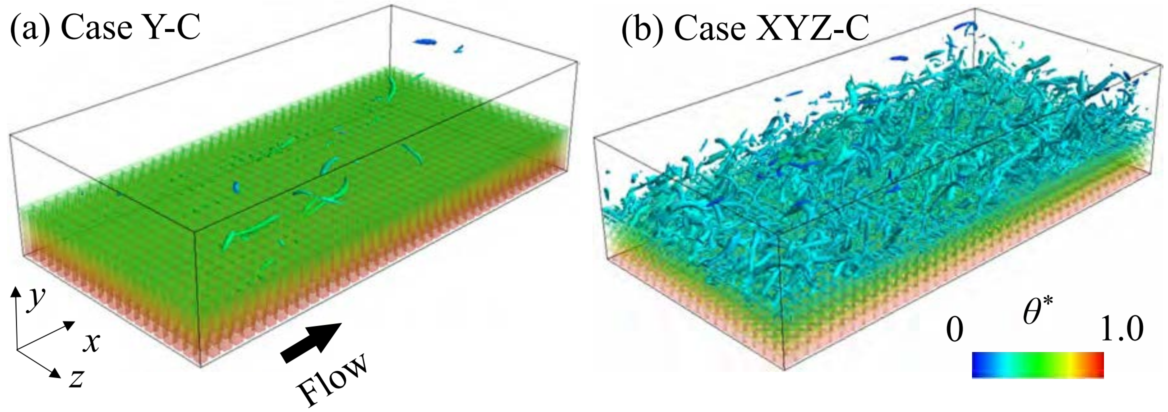
(a) Case Y-C
(b) Case XYZ-C
y
x
z
Flow
0
θ*
1.0

Figure 3: Snapshot of iso-surfaces of the second invariant of the velocity gradient tensor $II^* = 15$ colored by the local instantaneous temperatures $0 < \theta^* < 1.0$: (a) case Y-C and (b) case XYZ-C.

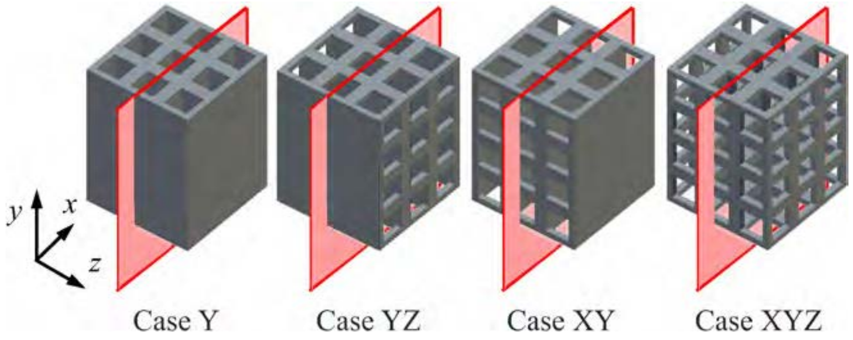
y
x
z
Case Y
Case YZ
Case XY
Case XYZ

Figure 4: Location of the visualized x–y planes.

(a) Case Y-I

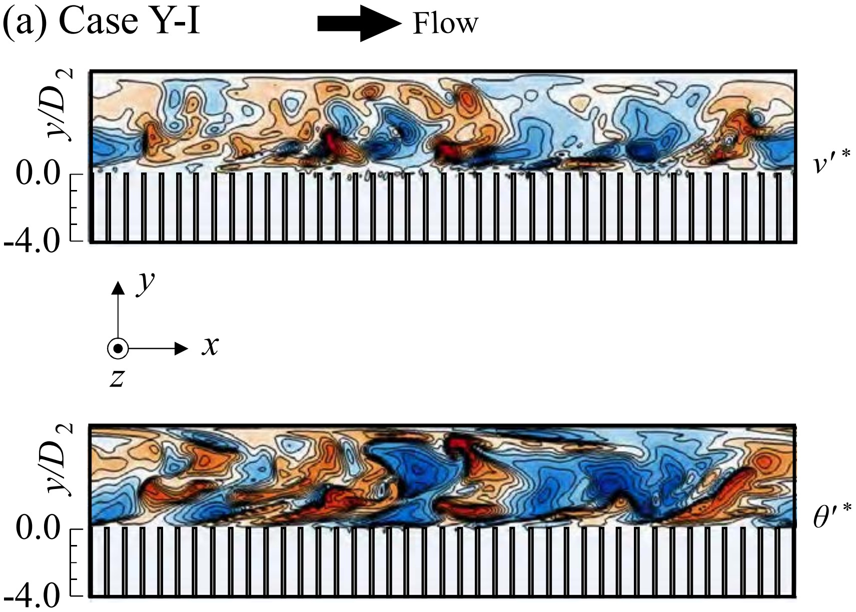

(b) Case YZ-I

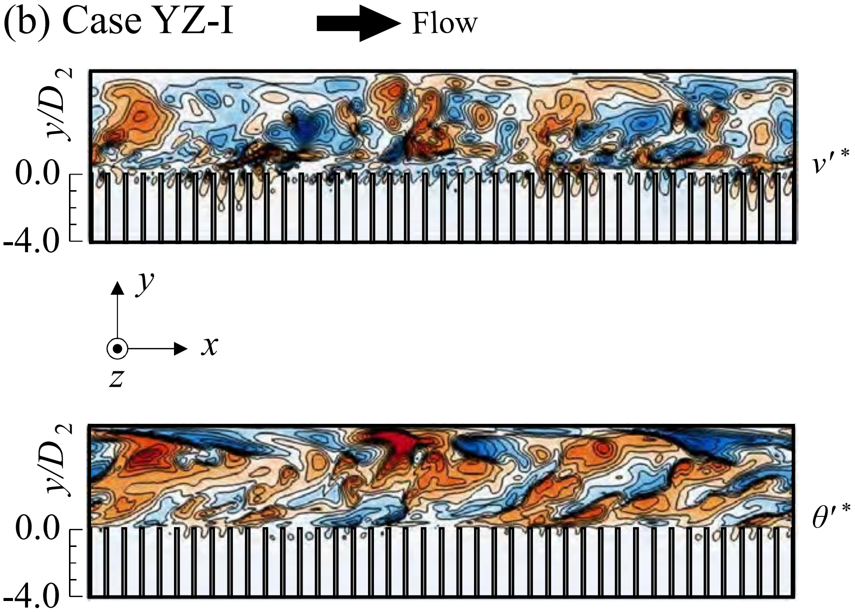

(c) Case XY-I

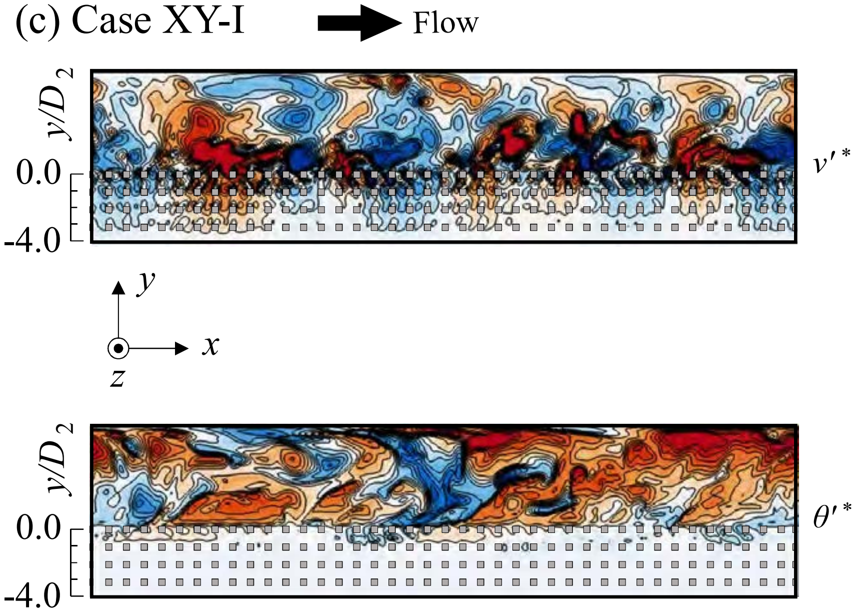

(d) Case XYZ-I

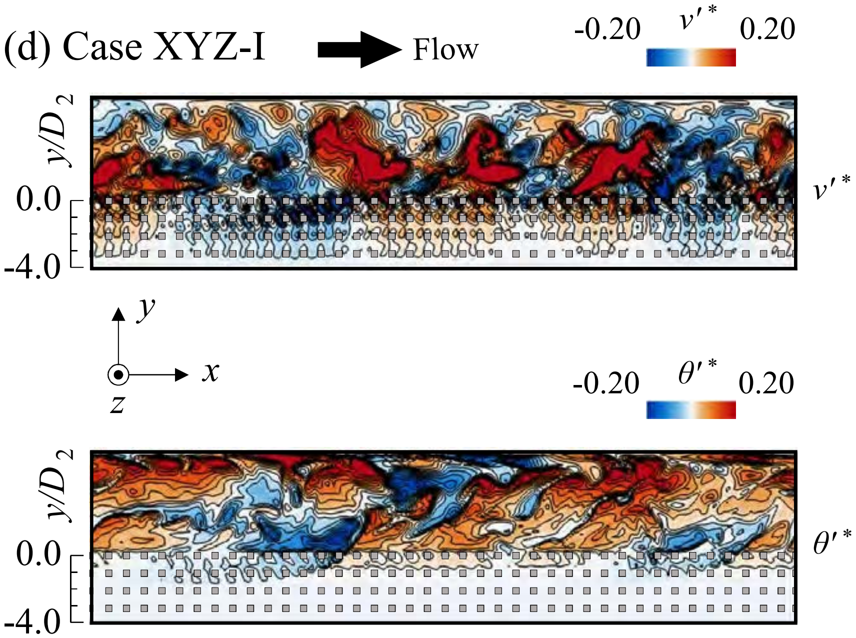

Figure 5: Snapshot of instantaneous vertical velocity and temperature fluctuations in isothermal wall boundary condition: (a) case Y-I, (b) case YZ-I, (c) case XY-I, and (d) case XYZ-I.

(a) Case Y-C

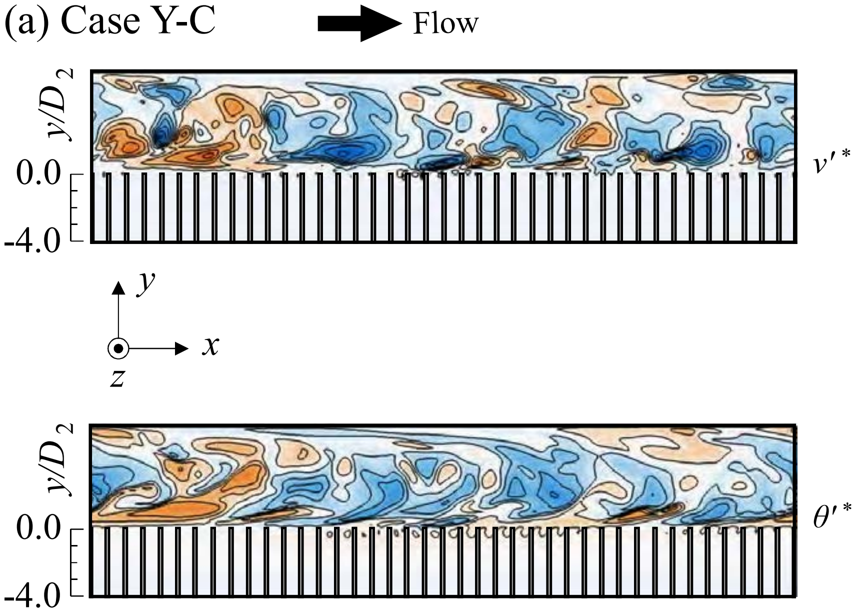

(b) Case YZ-C

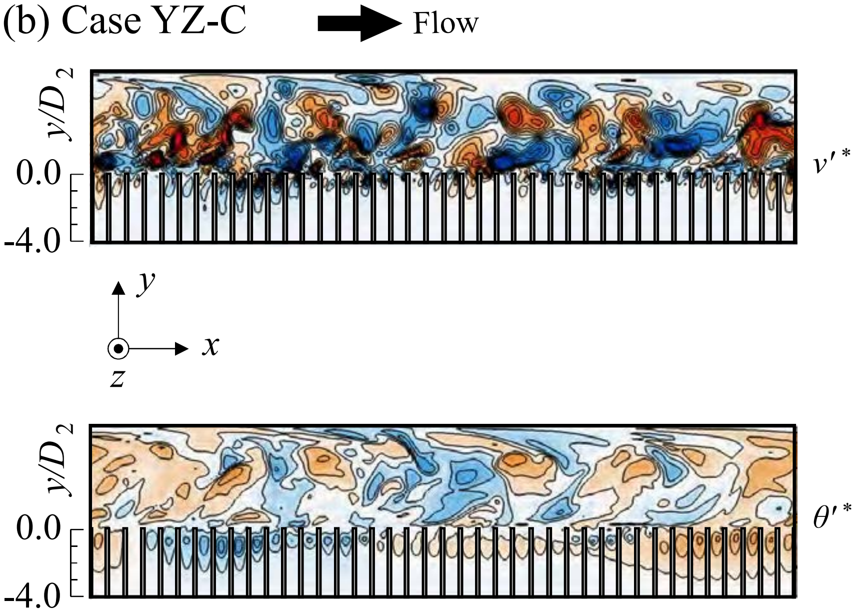

(c) Case XY-C

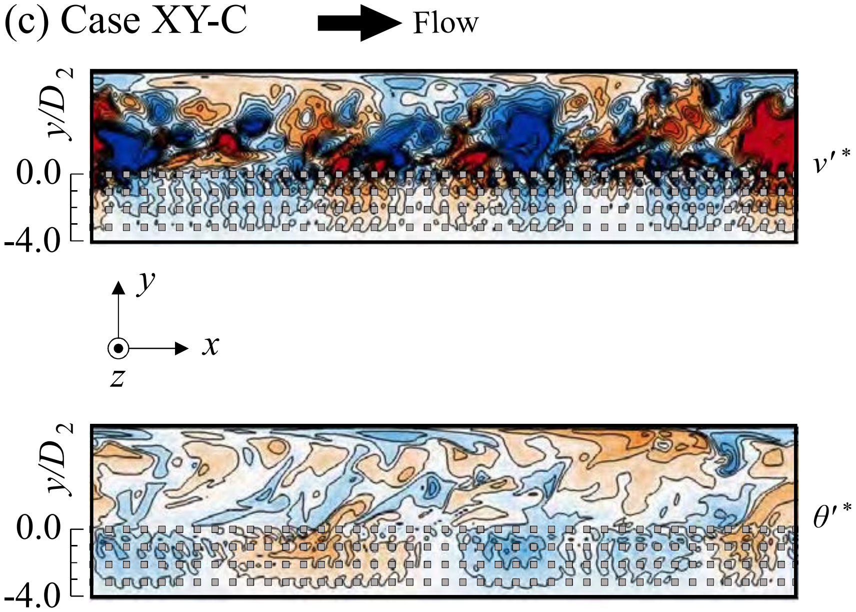

(d) Case XYZ-C

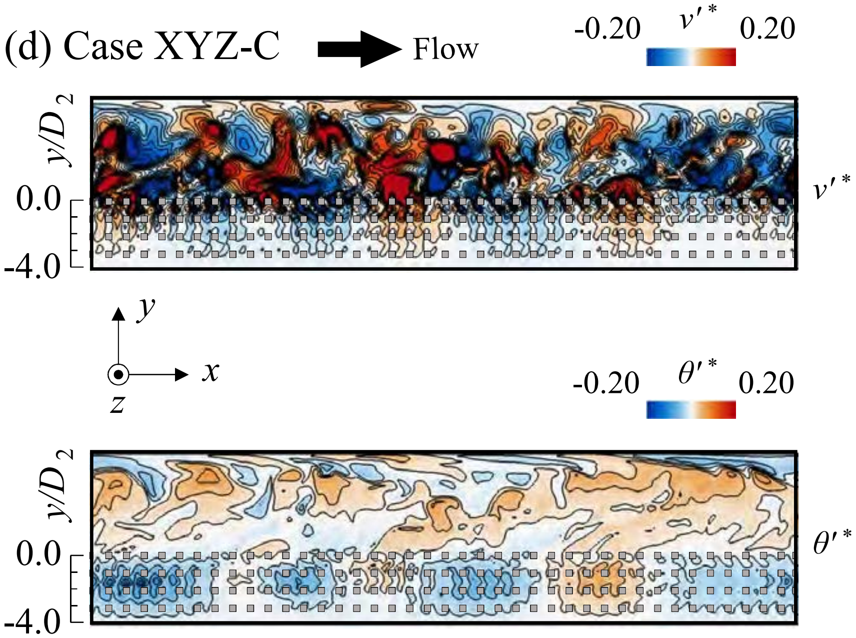

Figure 6: Snapshot of instantaneous vertical velocity and temperature fluctuations in conjugate wall boundary condition: (a) case Y-C, (b) case YZ-C, (c) case XY-C, and (d) case XYZ-C.

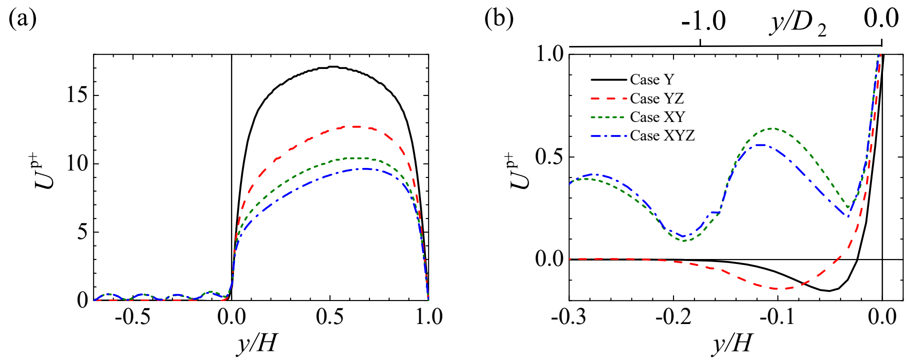

Figure 7: Plane-averaged streamwise mean velocity profiles: (a) in the overall region and (b) near the porous interface.

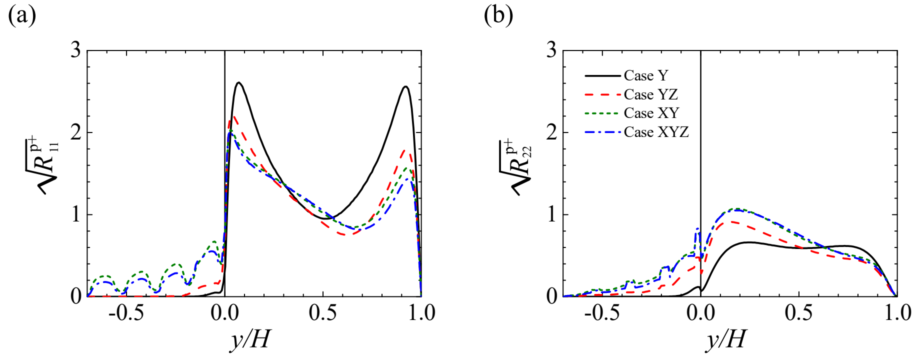

Figure 8: Plane-averaged Reynolds normal stresses: (a) streamwise component and (b) wall-normal component.

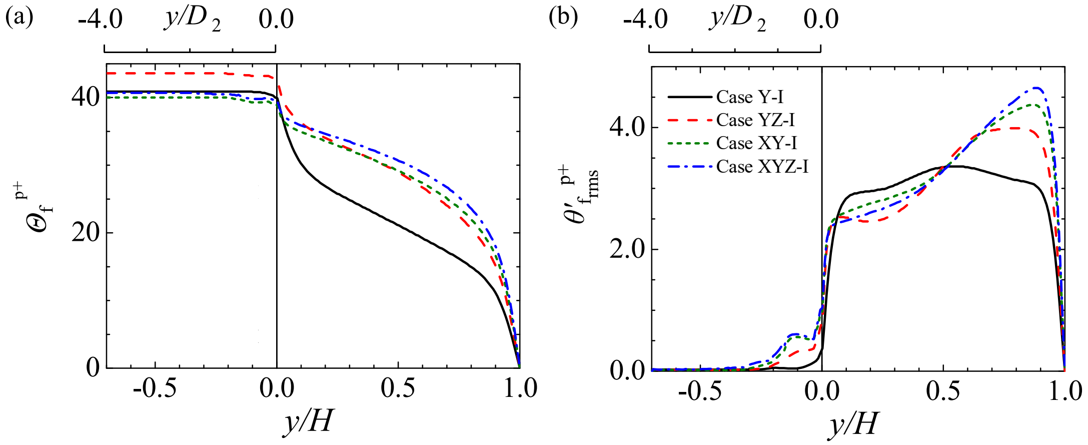

Figure 9: Plane-averaged mean and root mean square temperature profiles for the isothermal case: (a) mean temperature and (b) root mean square temperature.

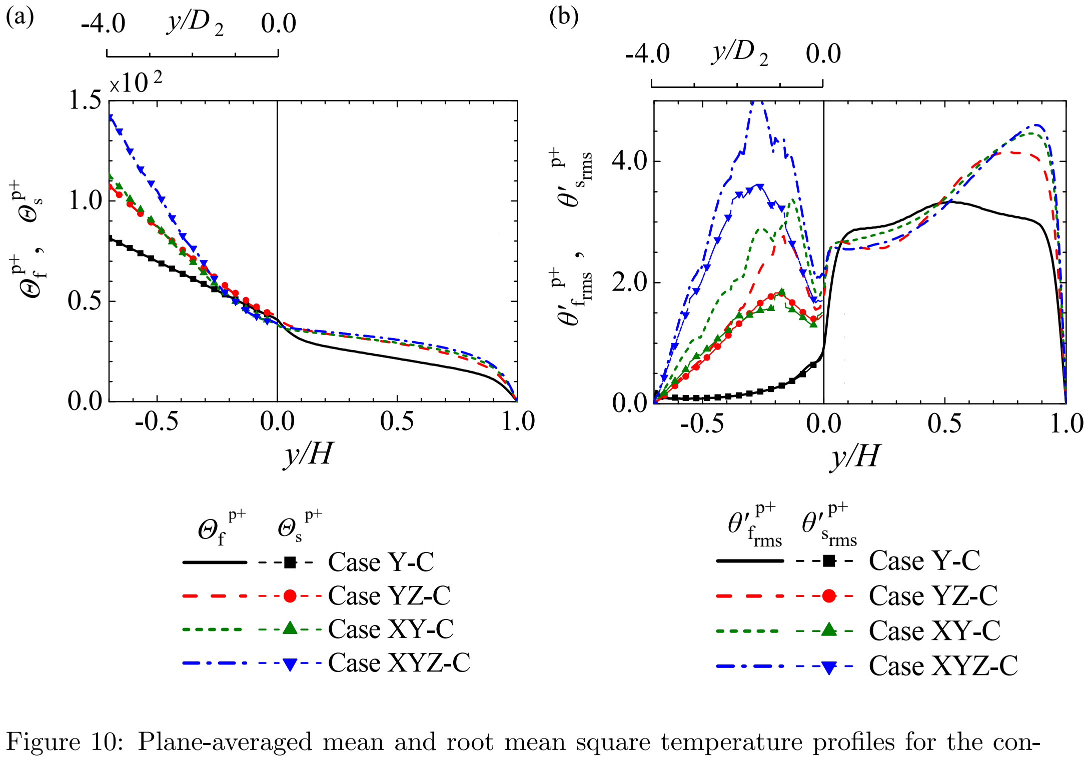

Figure 10: Plane-averaged mean and root mean square temperature profiles for the conjugate heat transfer case: (a) mean temperature and (b) root mean square temperature.

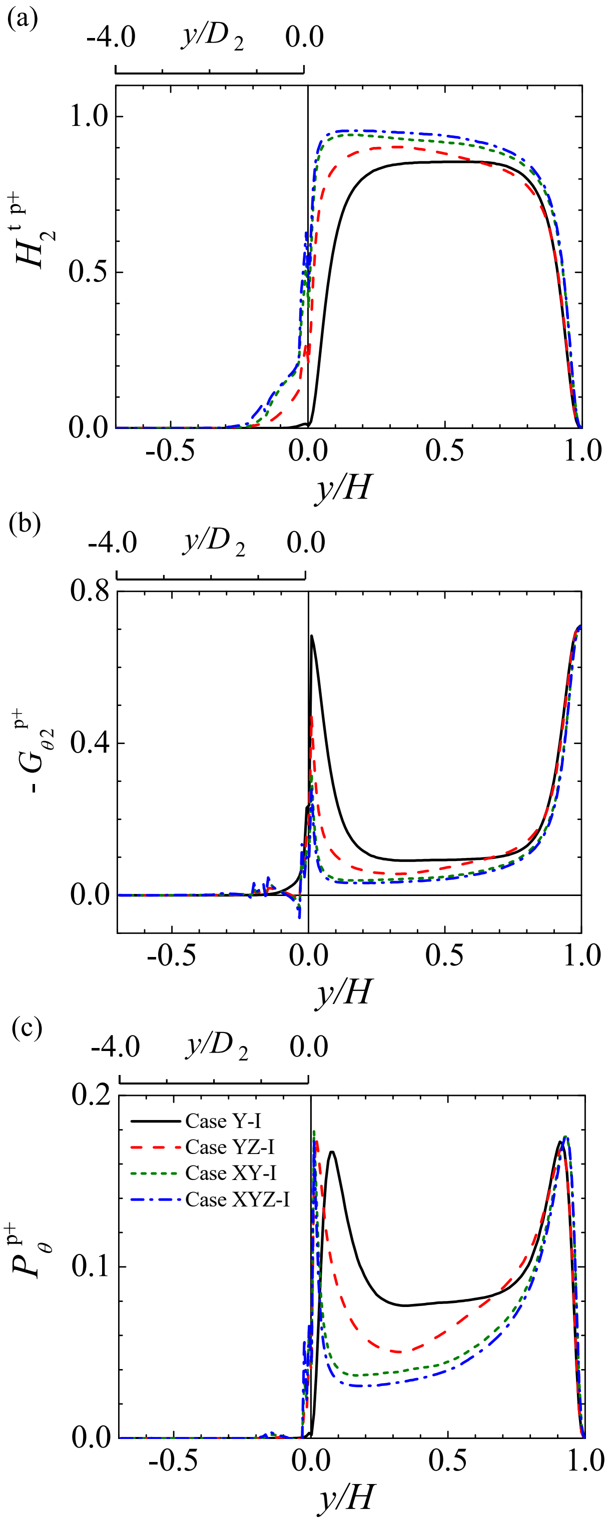

Figure 11: Plane-averaged vertical turbulent heat flux, vertical temperature gradient, and production of the temperature variance for the isothermal case: (a) vertical turbulent heat flux, (b) vertical temperature gradient, and (c) production of the temperature variance.

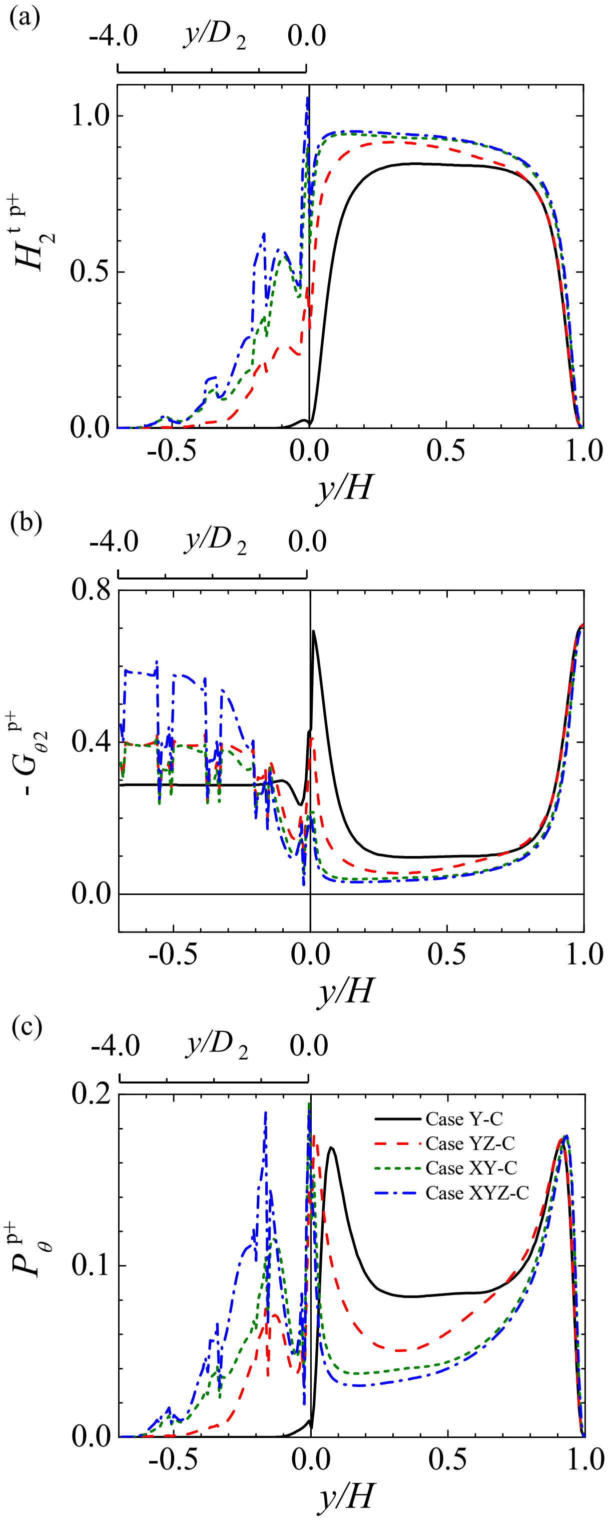

Figure 12: Plane-averaged vertical turbulent heat flux, vertical temperature gradient, and production of the temperature variance for the conjugate heat transfer case: (a) vertical turbulent heat flux, (b) vertical temperature gradient, (c) production of the temperature variance.

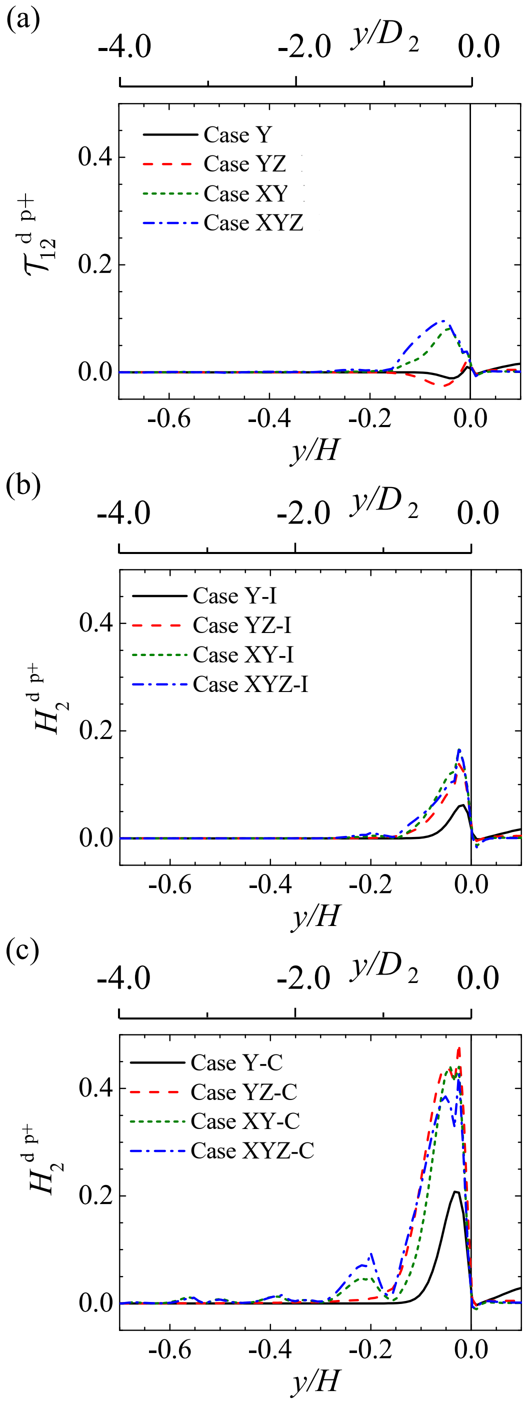

Figure 13: Plane-dispersion stress and vertical dispersion heat flux profiles: (a) plane-dispersion stress, (b) vertical dispersion heat flux for the isothermal case, (c) vertical dispersion heat flux of the conjugate heat transfer case.

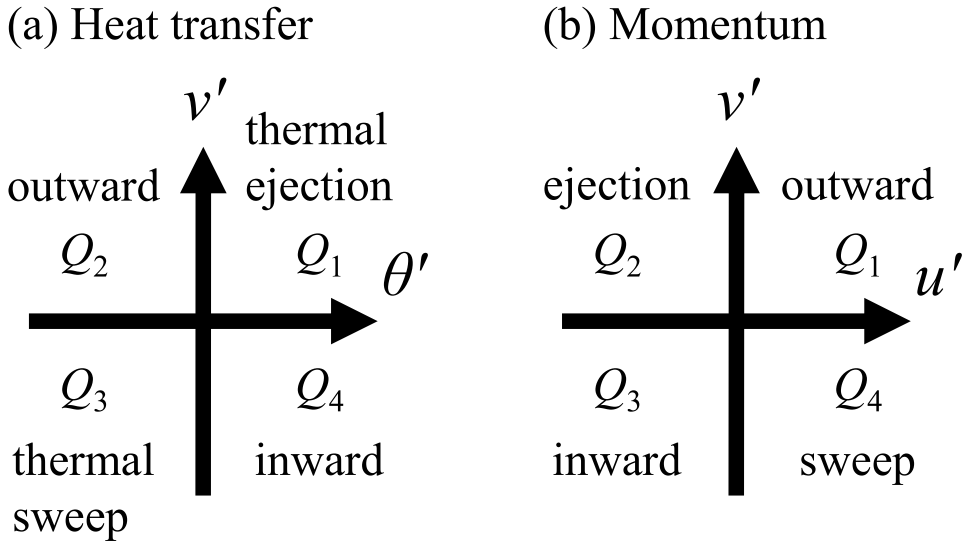
(a) Heat transfer
v'
thermal ejection
outward
Q_2
Q_1
θ'
Q_3
Q_4
thermal sweep
inward
(b) Momentum
v'
ejection
outward
Q_2
Q_1
u'
Q_3
Q_4
inward
sweep

Figure 14: Ejection-sweep definitions for heat and momentum transport: (a) heat transport and (b) momentum transport.

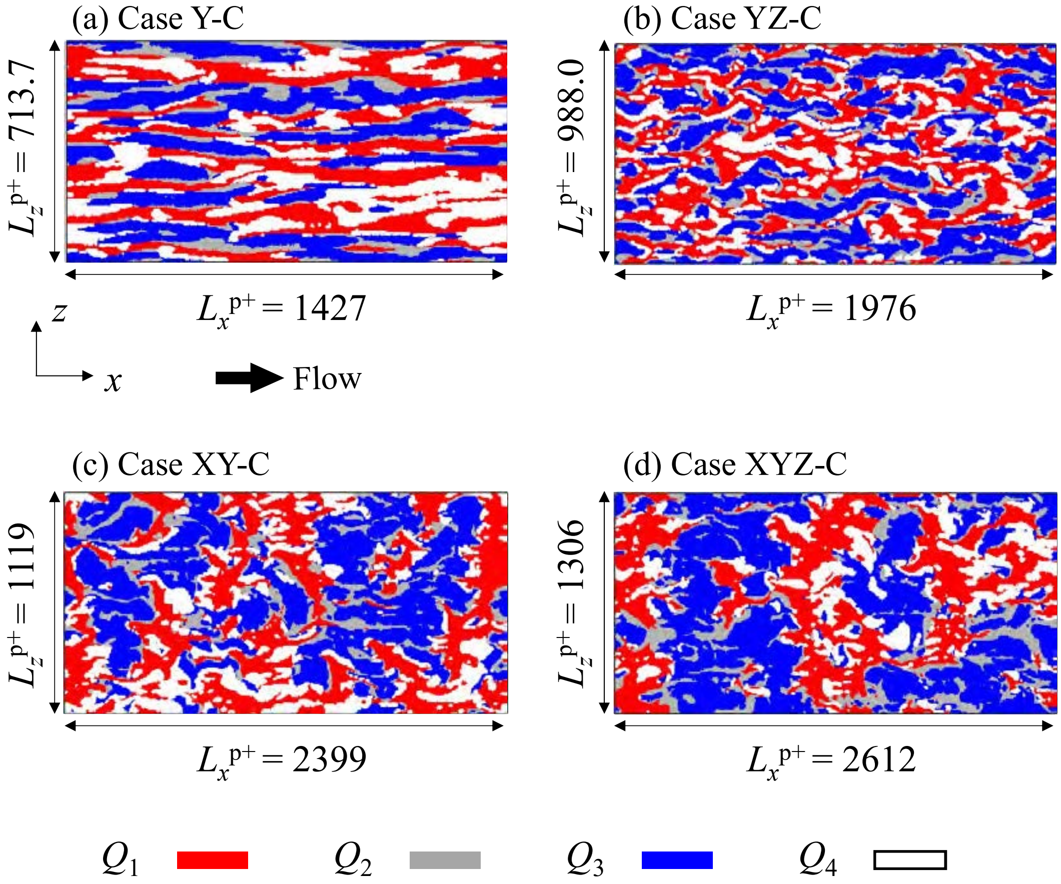

Figure 15: Snapshots of instantaneous quadrant events at $y^{\mathrm{p}+} = 13$ in the conjugate heat transfer condition: (a) case Y-C, (b) case YZ-C, (c) case XY-C, and (d) case XYZ-C.

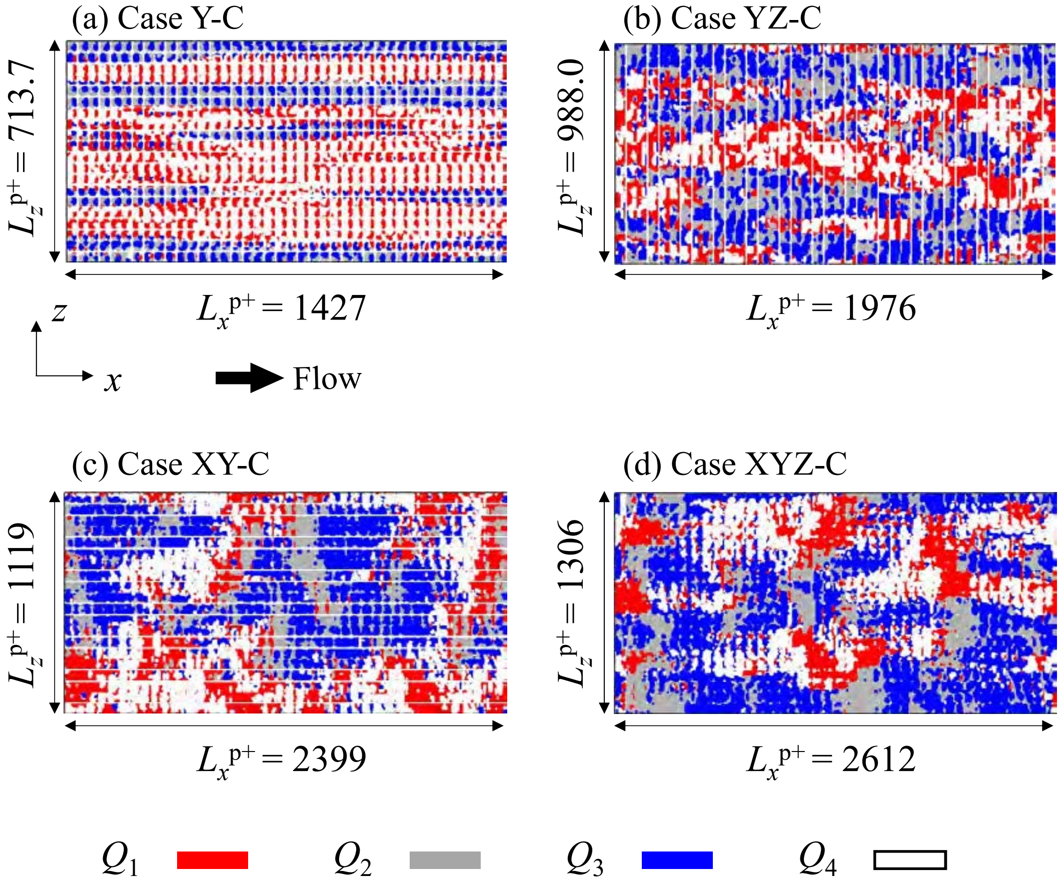

Figure 16: Snapshots of instantaneous quadrant events at $y^{\mathrm{p}+} = -14$ in the conjugate heat transfer condition: (a) case Y-C, (b) case YZ-C, (c) case XY-C, and (d) case XYZ-C.

(a) Case Y-I

(b) Case YZ-I

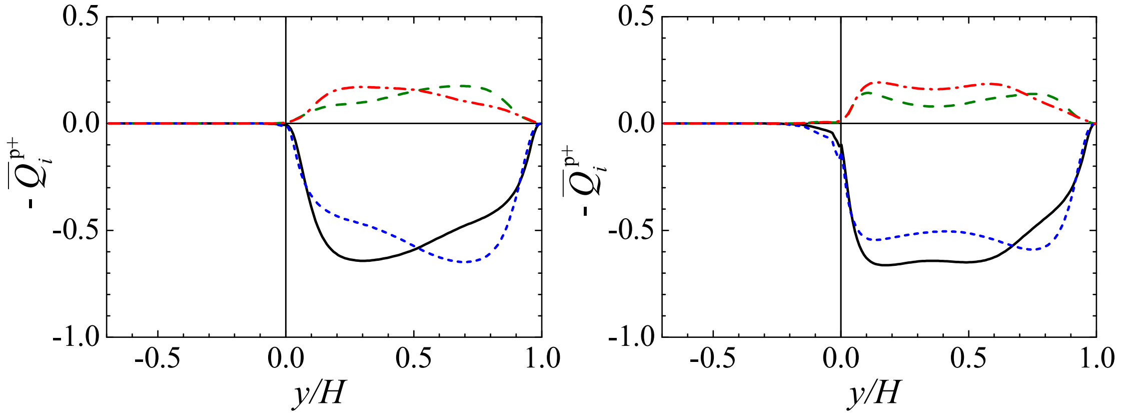

(c) Case XY-I

(d) Case XYZ-I

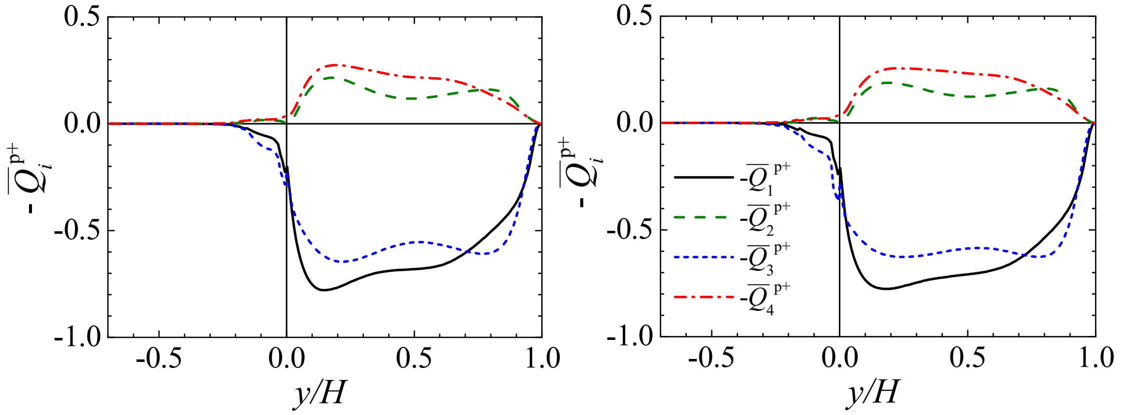

Figure 17: Plane-averaged quadrant contributions in isothermal wall boundary condition: (a) case Y-I, (b) case YZ-I, (c) case XY-I, and (d) case XYZ-I.

(a) Case Y-C

(b) Case YZ-C

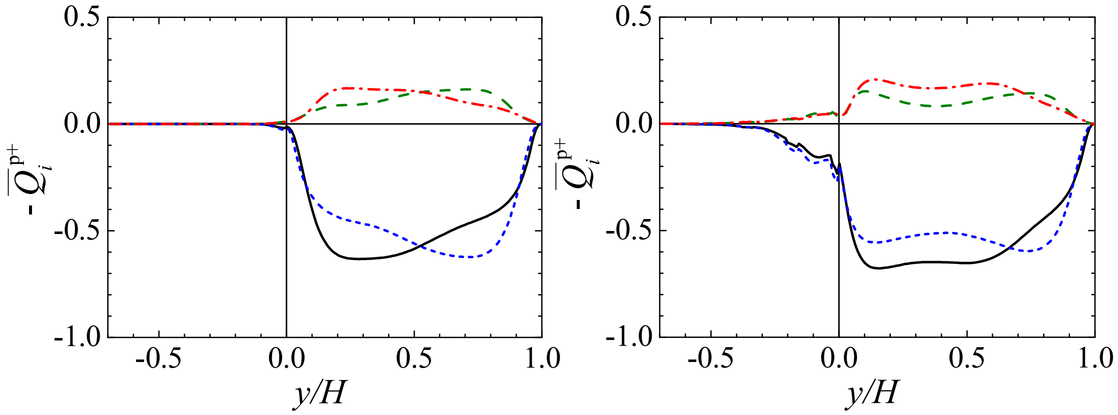

(c) Case XY-C

(d) Case XYZ-C

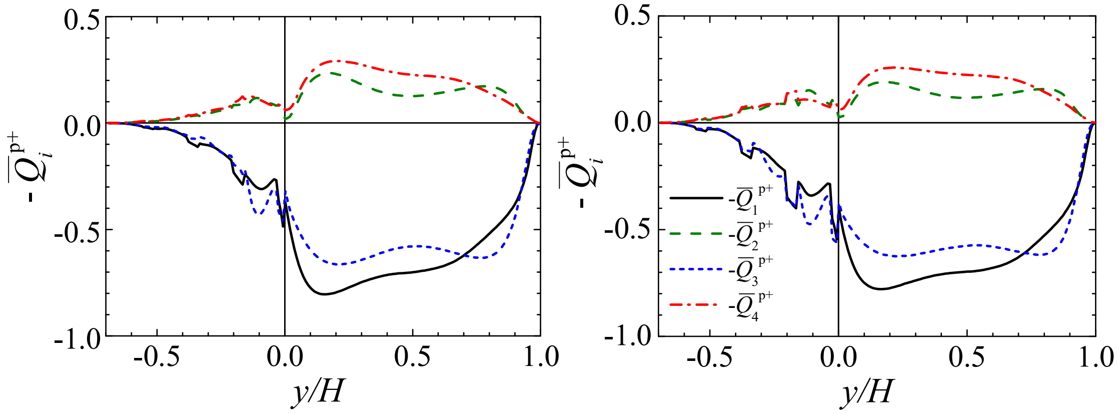

Figure 18: Plane-averaged quadrant contributions in conjugate heat transfer condition: (a) case Y-C, (b) case YZ-C, (c) case XY-C, and (d) case XYZ-C.

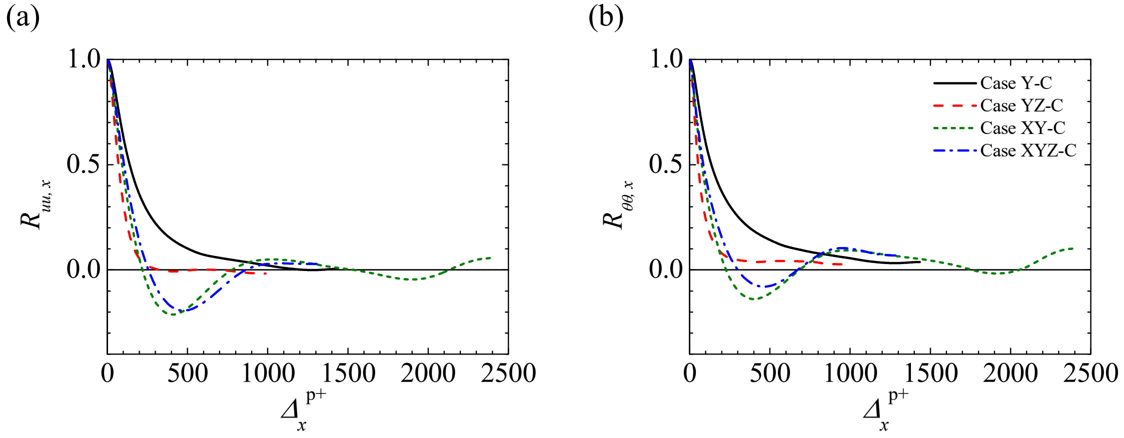

Figure 19: Streamwise two-point spatial correlation function for the conjugate heat transfer case: (a) streamwise velocity fluctuations and (b) temperature fluctuations.

(a) Case Y-C

(b) Case YZ-C

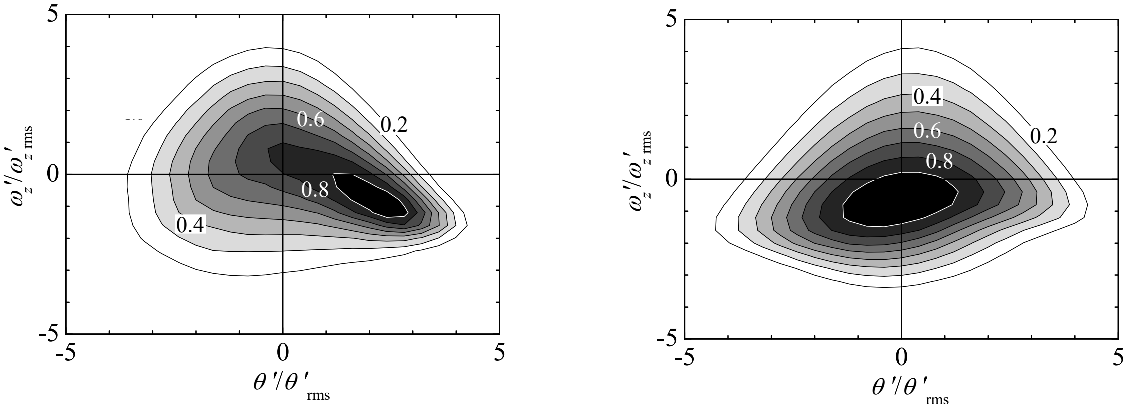

(c) Case XY-C

(d) Case XYZ-C

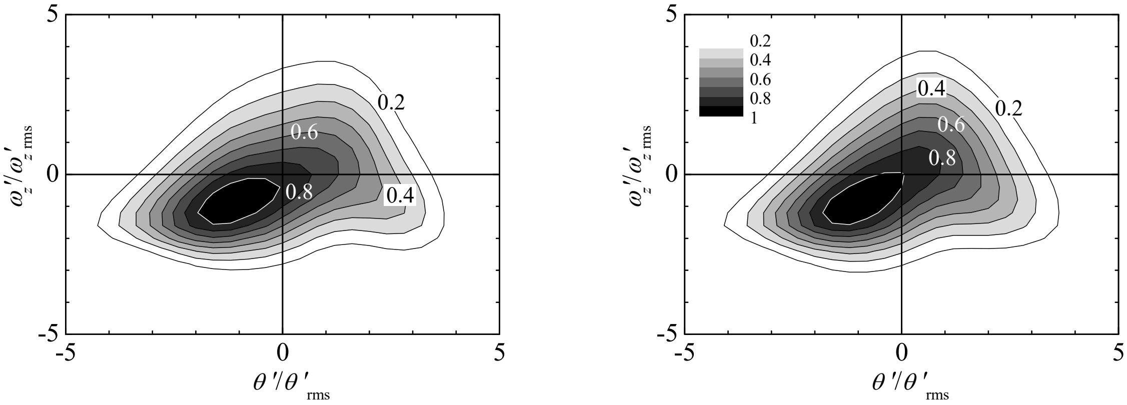

Figure 20: Joint probability density function $p(\theta', \omega'_z)$ of the fluctuating temperature and spanwise vorticity at $y^{\mathrm{p}+} \simeq 13$ for the conjugate heat transfer case: (a) case Y-C, (b) case YZ-C, (c) case XY-C, and (d) case XYZ-C.

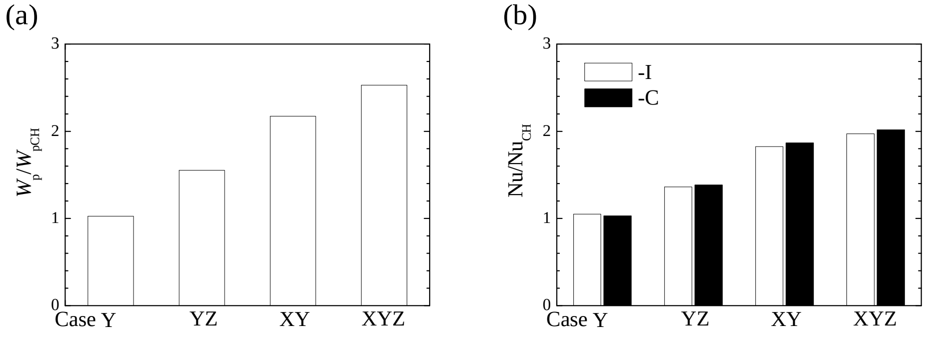

Figure 21: Heat transfer performance: (a) pumping power coefficient, (b) Nusselt number; W_{pCH} and $\mathrm{Nu}_{\mathrm{CH}}$ are the pumping power coefficient and Nusselt number of the plane channel at $\mathrm{Re}_{\mathrm{b}} = 2900$, respectively.

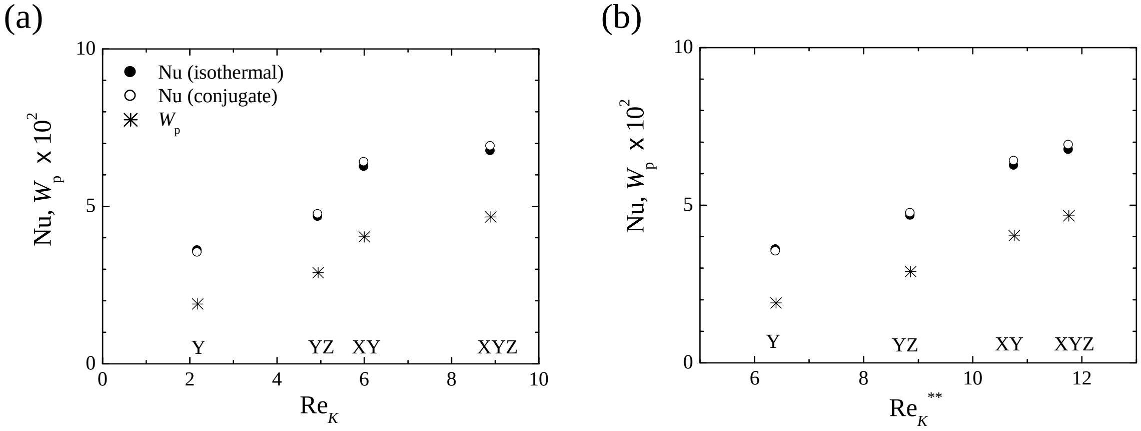

Figure 22: Pumping power coefficient and Nusselt number against the permeability Reynolds numbers: (a) correlation with the permeability Reynolds number Re_K and (b) correlation with the surrogate permeability Reynolds number Re_K^{**}.

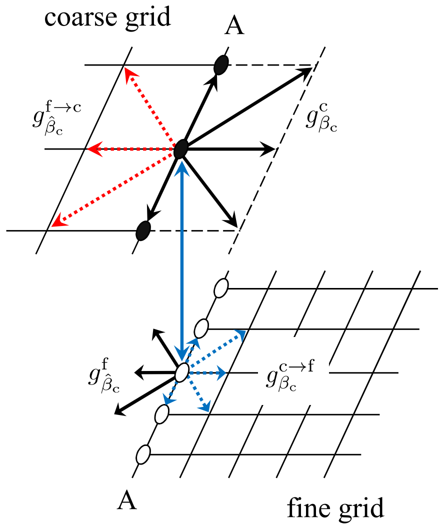
coarse grid
A
$g^{\mathrm{f}\rightarrow\mathrm{c}}_{\hat{\beta}_\mathrm{c}}$
$g^{\mathrm{c}}_{\beta_\mathrm{c}}$
$g^{\mathrm{f}}_{\hat{\beta}_\mathrm{c}}$
$g^{\mathrm{c}\rightarrow\mathrm{f}}_{\beta_\mathrm{c}}$
A
fine grid

Figure 23: Schematic of a face-to-face grid arrangement.

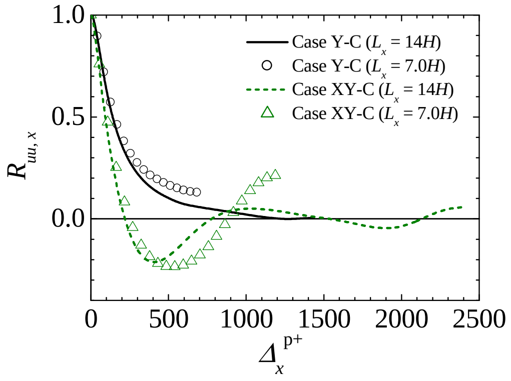

Figure 24: Streamwise two-point spatial correlation function of the streamwise velocity fluctuations in cases Y and XY.

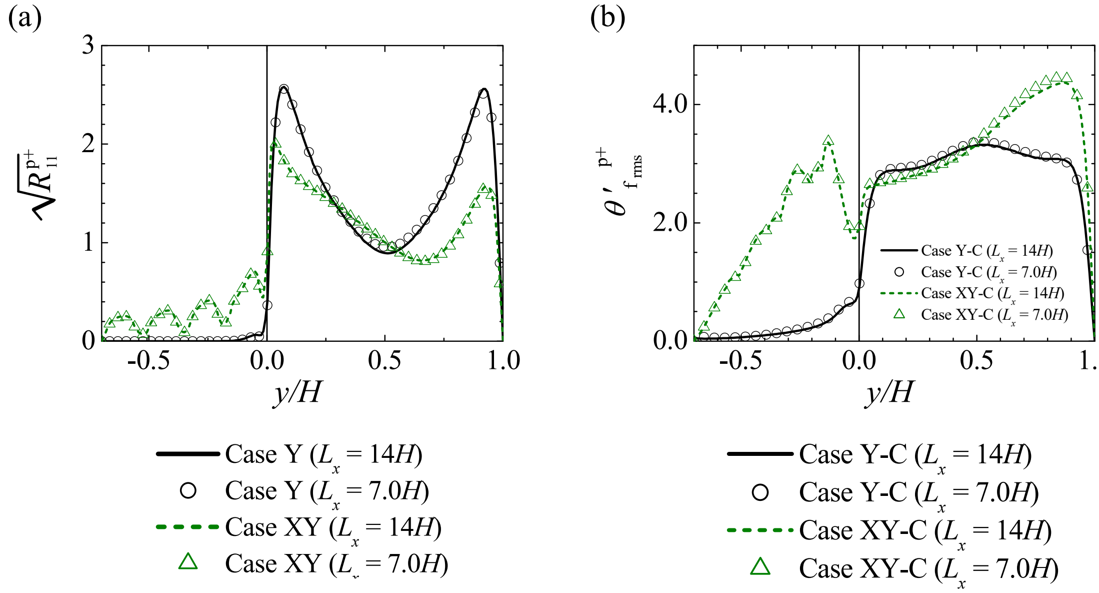

Figure 25: Plane-averaged streamwise Reynolds normal stress and root mean square fluid temperature in cases Y-C and XY-C: (a) streamwise Reynolds normal stress, (b) root mean square fluid temperature.